Climatology of Coherent Structures on the Extratropical Tropopause

GREGORY J. HAKIM*

National Center for Atmospheric Research,+ Boulder, Colorado

(Manuscript received 10 August 1998, in final form 19 February 1999)

ABSTRACT

This paper poses and tests the hypothesis that some of the synoptic-scale and mesoscale tropopause-based disturbances that produce organized vertical motion and induce surface cyclones in the extratropical troposphere are vortexlike coherent structures. Based on the theory of nonlinear waves and vortices, tests are constructed and applied to observations of relative vorticity maxima for a 33-winter climatology at 500 hPa and three-dimensional composites for a single winter season. The method is designed to determine the following disturbance properties: nonlinearity, quasigeostrophic potential vorticity–streamfunction relationship, speed, and trapping of fluid particles. These properties are determined for four disturbance-amplitude categories, defined here in terms of 500-hPa relative vorticity.

The results show that, on average, 500-hPa relative vorticity maxima are localized monopolar vortices with length scales (radii) of approximately 500–800 km; there is a slight increase in length scale with disturbance amplitude. Nonlinearity is $O(1)$ or greater for all amplitude categories, approaching $O(10)$ for the strongest disturbances. Trapping of fluid particles, estimated by the presence of closed contours of potential vorticity on isentropic surfaces near the tropopause, requires greater than $O(1)$ nonlinearity; the threshold disturbance amplitude is approximately 8×10^{-5} s^{-1} in the vertical component of 500-hPa relative vorticity and -8 K in anomaly tropopause potential temperature. The vortices move westward with respect to the background flow, with a slight northward drift. The observational evidence does not support an interpretation of these features in terms of modons or solitary waves.

1. Introduction

Extratropical cyclones and their life cycles have attracted considerable attention because of their importance to both daily weather patterns and the general circulation of the earth's climate system. Theoretical and idealized modeling studies have identified baroclinic instability of the vertically sheared quasigeostrophic (QG) flow of midlatitudes as the mechanism that gives rise to cyclone disturbances; the preferred scale of these unstable waves is approximately zonal wavenumbers 6–9, or wavelengths of approximately 3400–5000 km at 45° lat. Analyses of observed time series confirm the existence of these Rossby waves (RWs).[1] Other observational work, notably case studies, has identified long-lived and large-amplitude tropopause-based disturbances as being important to cyclogenesis (e.g., Sanders 1986; Hakim et al. 1996; Bosart et al. 1996). Motivated by the case study evidence, this paper explores the hypothesis that some of the tropopause-based disturbances are vortexlike coherent structures (CSs) that have properties quite different from the quasi-linear RWs. The goal of this study is to develop tests based on the theory of nonlinear waves and vortices and to apply these tests to observations to determine the veracity and generality of the vortex hypothesis.

The modern paradigm for extratropical cyclogenesis can be summarized in terms of two components: baroclinic instability and RW radiation. The idealized QG analytical linear baroclinic instability theories of Charney (1947) and Eady (1949) have been extended to the

* Current affiliation: Department of Atmospheric Sciences, University of Washington, Seattle, Washington.

+ The National Center for Atmospheric Research is sponsored by the National Science Foundation.

Corresponding author address: Dr. Gregory J. Hakim, Department of Atmospheric Sciences, Box 351640, Seattle, WA 98195.
E-mail: hakim@atmos.washington.edu

[1] In simplest form, the Rossby wave is a solution of the linear nondivergent barotropic vorticity equation on a β plane; the dynamics of the wave are controlled by the strength of the potential vorticity gradient (i.e., β). Following Hoskins et al. (1985) and Guinn and Schubert (1993), the term Rossby wave is used here more generally to refer to an oscillation due to gradients of Ertel (and QG) potential vorticity. A description of this generalization is given by Hoskins et al. (1985; section 6).

primitive equations, spherical geometry, and more realistic vertical wind profiles (Gall 1976a,b; Simmons and Hoskins 1976, 1977). The unstable modes of these generalized models agree broadly with the predictions of linear QG theory; Simmons and Hoskins (1976) found a growth rate maximum around zonal wavenumbers 6–9. Observational evidence confirming the existence of synoptic-scale RWs has been demonstrated by bandpass-filtered (e.g., 2.5–6 days) time series (e.g., Blackmon 1976; Blackmon et al. 1977; Blackmon et al. 1984a,b; Wallace et al. 1988; Lim and Wallace 1991). The results of these studies show waves that have wavelengths near 4000 km, westward tilt with height, and eastward phase speeds of 12–15 m s^{-1}.

It should be noted that the baroclinic instability component of the modern paradigm is not embraced unanimously. An alternative growth mechanism is transient (nonmodal) baroclinic amplification, which involves a combination of one or more, perhaps neutral, modes (e.g., Farrell 1984). Transient amplification enriches the possibilities for disturbance growth and provides for greater short-term growth than can be accounted for by a single unstable normal mode. Nonmodal growth also accounts for the structural transience typical of observed cyclogenesis events; such structural changes are not captured by a single unstable mode. Moreover, Farrell (1985, 1989) argued that in the presence of surface damping, such as an Ekman boundary layer, growth due to the unstable normal modes may be substantially reduced or eliminated entirely, whereas nonmodal growth involving the spectrum of neutral modes is still available for disturbance amplification.

Regarding the RW radiation component of the modern paradigm, Simmons and Hoskins (1979) studied the behavior of an initially localized disturbance defined by a 22.5° ''window'' of a zonal-wavenumber-8 unstable mode. The resultant evolution shows a developing wave packet with downstream and upstream RW radiation at the tropopause and surface, respectively. Similar behavior occurs for the Eady model, with the leading fringe of the disturbance moving at the speed of the background wind. Simmons and Hoskins concluded that downstream development can play an important role in the generation of upper-level disturbances that can proceed to trigger other baroclinic developments. Idealized modeling by Orlanski and Chang (1993) and Chang and Orlanski (1993) emphasizes the importance of downstream development to the generation of upper-level cyclogenesis precursor disturbances and the extension of storm tracks downstream from the region of greatest baroclinicity. Observational evidence confirming the importance of downstream development to cyclogenesis precursor disturbances involves individual case studies (Orlanski and Katzfey 1991; Orlanski and Sheldon 1993; Orlanski and Sheldon 1995; Nielsen-Gammon and Lefevre 1996) and time series analysis of 300-hPa meridional wind (Lee and Held 1993; Chang 1993).

A summary of the upper-precursor life cycle in the modern paradigm is summarized by the three-stage downstream baroclinic evolution schematic given in Orlanski and Sheldon (1995, their Fig. 3). The first stage involves the generation of an upper trough due to a downstream flux of energy (RW radiation) from a preexisting upstream upper trough. During the second stage, the new trough continues to grow due to downstream energy flux, but also strengthens due to baroclinic conversion associated with cyclogenesis (baroclinic instability). Finally, during the third stage the trough begins to decay due to a downstream flux of energy to yet another new trough. This picture is linked quite closely to linear theory, with nonlinear effects becoming important only when the disturbances reach large amplitude near the start of the occlusion phase of cyclogenesis (saturation).

A different perspective of cyclogenesis precursor disturbances is given by case studies, which show that the precursor can have large amplitude, localized structure, and exist well prior to surface cyclogenesis. The large amplitude and localized nature of cyclogenesis precursor disturbances is manifest in the potential vorticity (PV) distribution, which often appears as a horizontally narrow, downward extension of stratospheric PV (e.g., Uccellini et al. 1985; Boyle and Bosart 1986; Ogura and Juang 1990; Bleck 1990; Davis and Emanuel 1991; Reed et al. 1992; Hakim et al. 1995). Regarding the longevity of the precursor disturbance, Sanders (1988) subjectively tracked upper disturbances based on their signature in the 500-hPa height field and found that disturbance lifetimes have a mode of 5 days, although some last more than 30 days. An objective approach to the same problem by Lefevre and Nielsen-Gammon (1995) also shows a trough lifetime distribution with a tail toward larger values, but with a mean of 4 days. Additional evidence for long disturbance lifetimes comes from individual case studies. For the 25–26 January 1978 cyclogenesis over eastern North America, Hakim et al. (1996) tracked the precursor disturbances back at least 10 days, and for the 13 March 1993 cyclogenesis over eastern North America, Bosart et al. (1996) found that they are capable of being tracked for over 2 weeks.

An explicit demonstration of cyclogenesis associated with a localized vortex is given by Takayabu (1991, 1992). Takayabu studied idealized primitive equation initial-value problems for a vortex located on the tropopause and found robust surface cyclone development. Furthermore, Takayabu finds observational evidence for this type of development in 7 out of 39 rapidly developing western Pacific cyclones during 1986. Takayabu noted that there is a need for studies that focus on the upper vortex and that ''these vortices seem to be isolated disturbances rather than a crest of wave packets.'' Schär and Wernli (1993) studied cyclogenesis associated with localized tropopause potential temperature anomalies with uniform interior PV and find that a rapid surface

cyclogenesis ensues, with realistic surface frontal structure and airstreams reminiscent of observations.

Motivated by the importance of the upper-level precursor to surface cyclogenesis and observations showing that these disturbances can have large amplitude, localized structure, and long lifetimes, we address the hypothesis that some of these features may be more closely related to nonlinear coherent structures, such as vortices, than to the quasi-linear RWs. The goals here focus on determining the mean structure of disturbances that possess a primary attribute of the upper-level precursor disturbance: a midtropospheric vorticity maximum. Furthermore, we seek to understand how disturbance structure depends on amplitude. A brief overview of the characteristics of linear and nonlinear waves is given in section 2 to introduce the properties that distinguish linear waves from coherent structures. The method of data analysis is presented in section 3. Results for a 33-winter sample of 500-hPa vorticity maxima (hereafter, VM) over the Northern Hemisphere can be found in section 4 and the results for three-dimensional composites of 500-hPa vorticity maxima for a single winter near North America can be found in section 5. Conclusions are drawn in section 6.

2. Overview of linear waves and coherent structures

For the sake of simplicity and clarity in presentation, the following discussion regarding linear waves and nonlinear CSs will appeal to two-dimensional (barotropic) dynamics, and focus on comparing and contrasting properties of the solutions to motivate observational diagnosis. Consider the nondivergent barotropic vorticity equation on a β plane,

$$\zeta_t + J(\psi, \zeta) + \beta\psi_x = 0, \tag{1}$$

for an unbounded Cartesian geometry. The relative vorticity is given by $\zeta = \nabla^2\psi$; the vector wind is related to the streamfunction, ψ, by $\mathbf{V} = (u, v) = (-\psi_y, \psi_x)$; $J(a, b) = a_x b_y - a_y b_x$; and subscripts denote partial differentiation. To determine the relative importance of individual terms in (1), nondimensional variables (denoted by a hat) are introduced: $(x, y) \sim L(\hat{x}, \hat{y})$, $(u, v) \sim U(\hat{u}, \hat{v})$, $\psi \sim UL\hat{\psi}$, $\beta \sim B\hat{\beta}$, and $t \sim (BL)^{-1}\hat{t}$. Substitution in (1) yields a nondimensionalized form of the nondivergent barotropic vorticity equation (dropping the hat notation):

$$\zeta_t + \beta\psi_x = -\delta_\beta J(\psi, \zeta). \tag{2}$$

Here, $\delta_\beta = U/BL^2$ is a parameter[2] that scales nonlinear effects associated with advection (e.g., Rhines 1975; Flierl 1977; Davey and Killworth 1984). In comparison, dispersive effects due to the planetary vorticity gradient, β, are $O(1)$.[3]

Linear theory results from (2) for $\delta_\beta \ll 1$, so that the righthand side of (2) can be neglected; the solutions are RWs. A localized initial condition will spread with time, reflecting the dispersive nature of RWs; the details of this evolution depend on the initial condition. A detailed examination of the linear barotropic initial-value problem is given by Pedlosky (1987, section 3.24), and Flierl (1977) examines the linear stratified-QG initial-value problem.

To counteract the dispersive nature of the linear dynamics and allow for long-lived CSs, some amount of nonlinearity must be incorporated. The remainder of this section focuses on three archetypical CS solutions, ordered with respect to increasing contributions from nonlinearity: solitary waves, modons, and monopolar vortices.

Allowing a small amount of nonlinearity in (2) permits weakly nonlinear solitary wave solutions. For completeness, a brief derivation of a solution is given in the appendix; the interested reader can find further details and generalized solutions in the review article by Malanotte-Rizzoli (1982) and in Haines and Malanotte-Rizzoli (1991). Four properties of the solitary wave solution (A.6) are the following.

- The propagation speed (c) depends on both the width (W) and amplitude (A) of the wave.
- A given background-flow profile supports either eastward moving (low over high in streamfunction) or westward moving (high over low in streamfunction) solitary waves (Malanotte-Rizzoli 1982).
- These solutions are highly anisotropic. For $\delta_\beta = 0.1$, the zonal length scale is roughly 3.2 times the meridional length scale.
- The disturbance structure is given by a relationship between the PV and the streamfunction.

This relationship is determined in part by the background flow through the solution of (A3).

These solitary waves are coherent and localized anisotropic vortex dipoles with weak and balancing nonlinearity and dispersion. Although they may provide a model for upper disturbances that appear as elongated jet streaks, they may not apply well for upper disturbances that are isotropic and predominantly monopolar.[4]

Relaxing the assumptions of weak nonlinearity and dispersion [i.e., $\delta_\beta \sim O(1)$] results in the theory of modons. For completeness, a brief derivation of a modon solution is given in the appendix; the interested reader can find further details in Larichev and Reznik (1976),

[2] This parameter is also known as a measure of RW steepness (Rhines 1975).

[3] Although $\beta = 1$ by its scaling definition, β is written explicitly to facilitate comparison with the dimensional equation.

[4] Isotropy in the length scales requires $\delta_\beta = (L/L_x)^2 = 1$, violating the assumption of weak nonlinearity; see appendix A for further details.

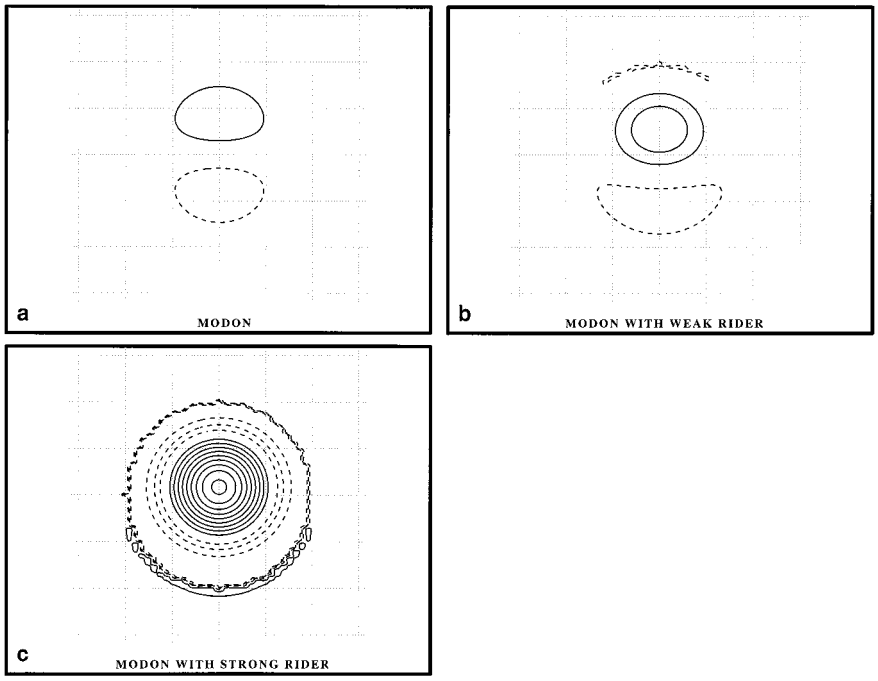

FIG. 1. Nondimensional relative vorticity for barotropic modons, with riders: (a) modon without rider [$\psi_R(0) = 0$], (b) modon with weak rider [$\psi_R(0) = -0.2$], and (c) modon with strong rider [$\psi_R(0) = -1$]. Modon wavenumbers are $k = 4.23244$ and $p = 3.16227$, corresponding to a speed $c = 1$. The nondimensional rider amplitude is given by $\psi_R(0)$. Dotted lines in all panels show the Cartesian grid every 0.5 nondimensional units. Scaling by $L = 1000$ km, $U = 10$ m s^{-1}, and $B = 1.5 \times 10^{-11}$ m^{-1} s^{-1} gives $\delta_\beta = 0.7$ and a vorticity scaling of 1.0×10^{-5} s^{-1}. Values are contoured every two units, and the zero contour is suppressed.

Flierl et al. (1980), and Kamenkovich et al. (1986). Examples of a modon with a rider (a monopolar vortex superposed on the modon) of varying amplitude are shown in Fig. 1. Although these three solutions appear quite different, they all share the same propagation speed; that is, the riders are dynamically passive. Four properties of the modon solutions (A9)–(A10) are the following.

- Barotropic modons move only eastward; however, shallow-water and stratified-QG modons can move westward at speeds greater than the gravest RW; that is, modon phase speeds are complementary to RW phase speeds.
- The structure is that of a cyclone-over-anticyclone vortex dipole.
- Like solitary waves, a modon's speed depends on both its amplitude and scale.
- The PV–streamfunction relationship is piecewise linear in the near and far fields. In addition, contours of $(\zeta + f)$ are closed within the modon so that fluid particles are trapped by and travel with the modon.

Finally, when nonlinearity is very strong, the left-hand side of (2) can be neglected in favor of the right-hand side. The resulting equation supports an infinite number of solutions of the form $\zeta = F(\psi)$. For monopolar vortices, there are a number of functionals, F, that are thought to describe realistic geophysical flows, including Gaussian vortices with length scale σ and amplitude A (e.g., Hopfinger and van Heijst 1993): $\psi = Ae^{-(r/\sigma)^2}$. As discussed by Flierl (1987), monopolar solutions are never *exactly* steady in the presence of β, although by the assumption $\delta_\beta \gg 1$ this unsteadiness is small compared to advection. Many aspects of general vortex dynamics are covered by Saffman (1992) and Hopfinger and van Heijst (1993), while the specific theory of QG vortices is reviewed by McWilliams (1991).

The nonlinear disturbances discussed here share three properties: significant nonlinearity (δ_β), a defining functional relationship between the streamfunction and the PV, and a connection between disturbance speed, length scale, and amplitude. This overview of linear and nonlinear wave theory motivates determination of the following properties for observed disturbances: the nonlinearity parameter (δ_β), the PV–streamfunction relationship, and the disturbance speed (relative to the background flow) as a function of scale and amplitude.

A brief review of generalizations to the barotropic solutions follows. Stratified-QG solitary wave solutions are given by Malanotte-Rizzoli (1982; see her Table 1), and have been proposed as models for periods of jet stream intensification and weakening (e.g., Haines and Malanotte-Rizzoli 1991; Haines et al. 1993). The barotropic modon solutions have been extended to incor-

TABLE 1. Scale estimates and nondimensional parameters for climatological anomaly fields. Disturbance parameters are maximum geostrophic wind speed, U_d (m s^{-1}), and length scale, L (km). Nondimensional parameters are nonlinearilty, $\delta_\beta = U_d/\beta L^2$ and $\delta = \zeta'/\overline{\zeta}$; magnitude of the background-flow total deformation, $\overline{D}$; and Rossby number, U_d/fL. Here, $f = 10^{-4}$ s^{-1} and $\beta = 1.5 \times 10^{-11}$ m^{-1} s^{-1}, and all values apply at 500 hPa.

Category	U_d	L	δ_β	δ	$\overline{D}$	Ro
Weak	6.4	525	1.5	1.9	0.3	0.12
Moderate	8.4	675	1.2	4.6	0.3	0.12
Strong	14	850	1.3	6.8	0.4	0.16
Extreme	23	850	2.1	9.6	0.4	0.27

porate realistic effects such as baroclinicity (e.g., Flierl et al. 1980; Berestov 1979, 1981; Kizner 1984), barotropic shear (Swenson 1982; Verkley 1987; Haupt et al. 1993), and spherical geometry (Tribbia 1984; Verkley 1984; Neven 1994). Overall, the results of these studies indicate that the modon is a robust solution in the sense that it exists in both barotropic and baroclinic flows, it is stable to small perturbations, and it appears to persist in the presence of weak horizontal shear. These encouraging results have suggested the application of modon solutions to observed phenomena. For example, the high-over-low modon has been proposed as a model for blocking (e.g., McWilliams 1980; Butchart et al. 1989; Ek and Swaters 1994). We note that the basic solution characteristics outlined earlier, such as the PV–streamfunction relationship (piecewise linear for the modons), the dependence of phase speed on scale and amplitude, and phase-speed constraints, also apply to the generalized solutions.

A generalization of the barotropic nonlinearity parameter, δ_β, is given by nondimensionalizing the QGPV equation for disturbance and background-flow variables. Under these conditions, it can be shown that nonlinearity scales as $\delta = U_0'/\overline{U}_0 \approx q_0'/\overline{q}_0$ [Shepherd 1987; Eq. (2.7)], where primes (overbars) indicate disturbance (background flow) quantities.[5] The approximation to the QGPV ratio (or, equivalently, vorticity ratio) gives an underestimate of δ for the usual situation in which the disturbance length scale is smaller than the background-flow length scale. Subsequent estimates of δ are given by the ratio of disturbance to background-flow vorticity, given the clean distinction between disturbance and background flow in this field.

3. Method

Previous studies have addressed the climatological properties of frequency, genesis, and lysis of upper-level disturbances, which are typically defined as local maxima in a vorticity-related quantity at 500 hPa (e.g., Sanders 1988; Lefevre and Nielsen-Gammon 1995; Dean and Bosart 1996). The theory for CSs outlined above motivates a climatology ordered by disturbance amplitude. As in previous investigations of upper-level perturbations, they are defined here as local maxima in the vertical component of relative vorticity at 500 hPa. A motivation for defining disturbances in terms of relative vorticity at 500 hPa arises from the fact that this choice of field and pressure level acts somewhat as a filter. The disturbances of interest represent downward protrusions of the tropopause. Viewed from a PV perspective, the stretching of stratospheric values of PV implied by the tropopause deflection produces anomalous cyclonic vorticity in both the near and far fields. At 500 hPa, which is normally below the tropopause, the feature of interest stands in sharper contrast to the surrounding vorticity field as compared to 250 hPa, for example, where relatively larger values of shear vorticity associated with the jet stream compete with the disturbance vorticity field. Note that highly anisotropic features, such as upper-level fronts, have not been explicitly removed by the method described below and can potentially participate in the results. Last, we note that other definitions for upper-level disturbances, such as maxima in curvature vorticity, may give results different than those shown here.

The primary goals of this paper regarding the *structure* of upper-level disturbances and their surrounding environment, and assessing the CS hypothesis are addressed by 1) a 33-winter climatology, and 2) a 1-winter composite. The 33-winter climatology focuses primarily to determine the mean synoptic-scale and planetary-scale flow patterns that accompany VM at 500 hPa. The detailed three-dimensional structure accompanying VM is taken up in the 1-winter composite study.

a. Thirty-three winter climatology at 500 hPa

Data for this climatology consist of the National Centers for Environmental Prediction (NCEP) twice-daily gridded 500-hPa geopotential height (hereafter referred to as height) field for winters (December–February, hereafter DJF) during 1957–89, and the vorticity is approximated by its geostrophic value. These data are obtained from the CD-ROM archive described by Mass et al. (1987) and consist of an octagonal grid on a polar stereographic map projection with a horizontal grid spacing of 381 km at 60°N. To avoid a bias toward any particular latitude, a local Coriolis parameter is used to compute the geostrophic relative vorticity. Allowing f to vary introduces an additional term to the familiar β-plane expression for the geostrophic vorticity: u_g/a cotΦ, where Φ is latitude and a is the planetary radius. For midlatitudes (e.g., 45°N) and $|u_g| < 60$ m s^{-1}, this term contributes less than 1×10^{-5} s^{-1} to the geostrophic relative vorticity. Given the smallness of this term under these conditions, it is neglected. With this

[5] In this nondimensionalization, δ_β^{-1} scales the linear dispersion term associated with β, as is the case in (2) for $t \sim L/U$.

approximation, the geostrophic relative vorticity on the polar stereographic map projection is given by

$$\zeta_g = \frac{m^2}{f}(\phi_{XX} + \phi_{YY}), \quad (3)$$

where ϕ is the geopotential, and X and Y are the grid coordinates. The map-scale factor, $m = (1 + \sin 60°)/(1 + \sin\Phi)$, is a function of latitude only. Equation (3) is evaluated by standard second-order finite differences.

Local maxima in the ζ_g field are determined by interpolating the ζ_g field onto a 2.5° lat × 2.5° long grid and then checking for local maxima over the region encompassing 20°–80°N; the lat–long grid facilitates a search for VM at specific latitudes. A grid point (i, j) is declared a local maximum if surrounding points $(i \pm k/\cos\Phi, j \pm k)$ all have ζ_g less than point (i, j). Parameter k is the number of grid points to search over in the meridional direction and is scaled by $(\cos\Phi)^{-1}$ in the zonal direction so that roughly equal physical distances are scanned in both zonal and meridional directions at all latitudes. Comparison of the results of this method with tests using fixed $k = 3$ in the zonal direction show little difference equatorward of 40°N and a meridional increase to roughly double the number of events at 70°N. Tests with integer values of k ranging over 1–5 indicate that the mean structure of the disturbances is insensitive to this parameter, although $k = 1$ fields have a large number of gridpoint maxima. Results of calculations for the disturbance length scale, described in more detail below in section 4b, show a range of 675–725 km for the moderate category at 40°N; the 50-km range is roughly 1/7 of the grid resolution. Hereafter, $k = 3$ is used.

Four subjectively determined categories are defined to stratify the ζ_g maxima by amplitude and will be referred to as *weak*, *moderate*, *strong*, and *extreme*. These labels correspond to $0 < \zeta_g \leq 4 \times 10^{-5}$ s^{-1}, 4×10^{-5} s$^{-1} < \zeta_g \leq 8 \times 10^{-5}$ s^{-1}, 8×10^{-5} s$^{-1} < \zeta_g \leq 12 \times 10^{-5}$ s^{-1}, and 12×10^{-5} s$^{-1} < \zeta_g \leq 30 \times 10^{-5}$ s^{-1},[6] respectively. For all winters during the period 1957–89, there are a total of 18 293 weak events, 60 292 moderate events, 36 829 strong events, and 16 524 extreme events, giving a total of 131 938 events. Height anomaly fields are determined by subtracting the 33-yr DJF mean height from the full height field for each event. The choice of four categories, although arbitrary, resolves the transition from quasi-linear disturbances to coherent structures. Although additional amplitude categories would perhaps better resolve the transition to coherent structures, the results would not differ qualitatively from those given herein. Moreover, other potential categorization schemes, such as categories with equal numbers of events, would give an irregular discretization with respect to amplitude.

Since the geostrophic vorticity is used in the climatology as a surrogate for the vorticity of the analyzed (total) wind, it is worthwhile to examine the accuracy of this approximation. A simple test is performed during the period January–February 1989, when the NCEP and European Centre for Medium-Range Weather Forecasts (ECMWF) (described in section 3b) datasets overlap. During this time period, 92% of the NCEP geostrophic-VM in the combined moderate, strong, and extreme categories have corresponding total-wind vorticity maxima in the ECMWF dataset located within 500 km. Note that since the geostrophic vorticity may overestimate the analyzed-wind vorticity, the VM categories for the climatology may not necessarily coincide with the VM categories for the ERICA-period composites; however, general properties involving relative amplitude, rather than specific categories, are likely to remain comparable.

The method given here is designed to address issues concerning the structure of VM as a function of amplitude, and to ascertain what flow features accompany these disturbances. Since individual disturbances are not tracked, the ''events'' are not necessarily independent. As such, individual disturbances may be sampled more than once, and in more than one category. This draws into question the appropriate number of degrees of freedom for computing statistical significance of the anomaly fields. Assuming an average lifetime of 5 days (Sanders 1988; Lefevre and Nielsen-Gammon 1995) implies an order of magnitude reduction in the number of degrees of freedom based on the number of events. With this assumption, the tests for statistical significance of the anomaly fields are essentially unchanged (not shown).

An alternative approach to the one taken here would be to track VM and develop composites at points along disturbance trajectories. Although this method could avoid multiple samples of individual disturbances, it is complicated by the fact that VM could fall into more than one amplitude category during their lifetime. Despite its shortcomings, the method outlined here provides a straightforward means to determine how VM structure varies with amplitude.

b. ERICA-period composites

The results of the analysis described in the previous section provide climatological documentation of synoptic and planetary-scale structure associated with VM at a single level. Resolution of the three-dimensional structure associated with VM requires use of a finer-scale dataset. Here we utilize data from the ERICA period, 1 December 1988–28 February 1989. These data are taken from the data assimilation system at ECMWF (Hollingsworth et al. 1986). The data consist of horizontal wind components, isobaric-coordinate vertical

[6] The upper bound of 30×10^{-5} s^{-1} is chosen arbitrarily, although it does act to filter spurious VM associated with erroneous 500-hPa height fields. The upper bound removes 62 such events, or 0.05% of all events, over the 33-yr period.

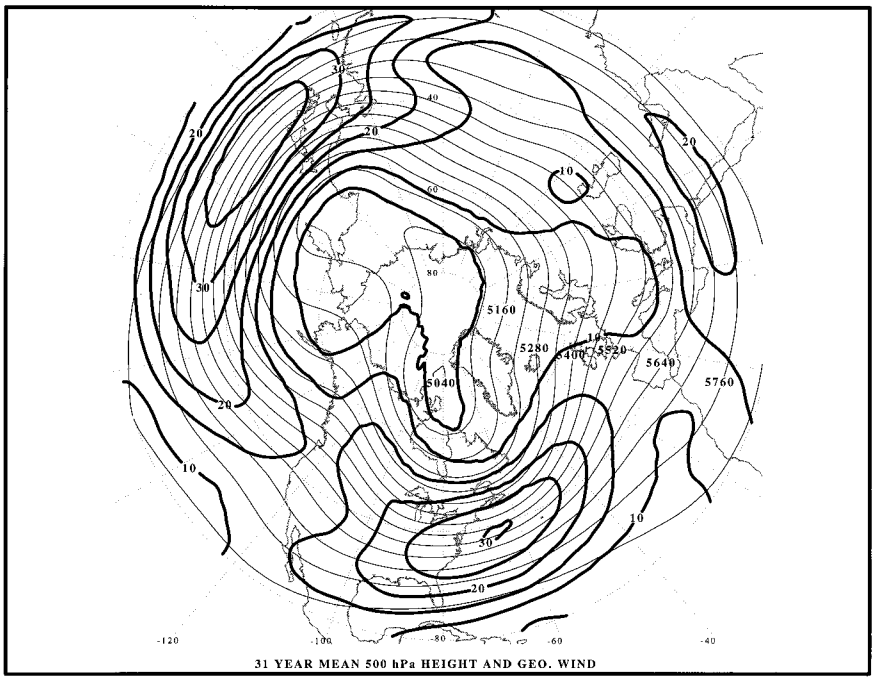

FIG. 2. Thirty-three-year mean DJF 500-hPa geopotential height (thin lines, every 60 m) and geostrophic wind speed (thick lines, every 5 m s^{-1}).

motion, temperature, and geopotential height. The data are available every 6 h at mandatory levels between 50 and 1000 hPa on a 1.125° lat × 1.125° long grid that is interpolated to a 1° × 1° grid.

The method of determining VM is the same as that described above, except for the use of the vertical component of relative vorticity of the total (analyzed) wind and the data area for compositing is a subset of the full data area: 30°–60°N and 60°–130°W. Composites are derived by averaging all events after interpolating to a common grid, with the VM centered at 45°N. The VM events for each category are used to construct three-dimensional composites of wind (u, v, and w), temperature, and Ertel potential vorticity (EPV). Anomaly fields are constructed from local values of 3-month mean fields and averaged as described previously.

Particular importance is attributed to distributions of EPV near the tropopause since gradients in this quantity are largest at this location, and disturbances are typically based near the tropopause. Thus, the CS test for closed EPV contours is considered most significant at tropopause level. The tropopause is defined here as the 1.5 × 10^{-6} m^2 K kg^{-1} s^{-1} (hereafter 1.5 PVU) surface.

c. Conditions for closed contours

Given the importance of closed material contours as a signature of particle trapping by CSs, it is instructive to consider what disturbance amplitude is required to produce closed contours in a given field, such as tropopause potential temperature. For simplicity, consider a function, f, that is composed of a background field that depends on y only, $\overline{f}$, and a disturbance field, f'. For f to have a local extremum implies $f_y = 0$,[7] or

$$f'_y = -\overline{f}_y. \tag{4}$$

Consider now the simple case where $\overline{f}_y = C$, where C is a constant, and where $f' = Ae^{-y^2/(2L^2)}$. Condition (4) implies that $A = CL^2y^{-1}e^{y^2/(2L^2)}$. In this case, the amplitude factor A is minimized for $y = L$, which gives

$$A = CLe^{1/2}. \tag{5}$$

Parameter C is estimated from the area-mean meridional gradient of the mean tropopause potential temperature field over the domain for the ERICA composites (Fig. 6); this gives $C = -1.39 \times 10^{-5}$ K m^{-1}. Anticipating the length scale to range over 300–600 km implies an anomaly amplitude range of −7 K to −14 K to produce a local minimum in the full tropopause potential temperature field, on average, for disturbances having a Gaussian structure.

4. Thirty-three winter climatology at 500 hPa

The DJF mean 500-hPa height and geostrophic wind speed for the period 1957–89 are shown in Fig. 2. Major troughs are located over eastern North America and the

[7] Of course, to actually see closed contours on a chart with a typical contour interval, the amplitude of f' must be even larger than the amplitude required to produce a local extremum in f.

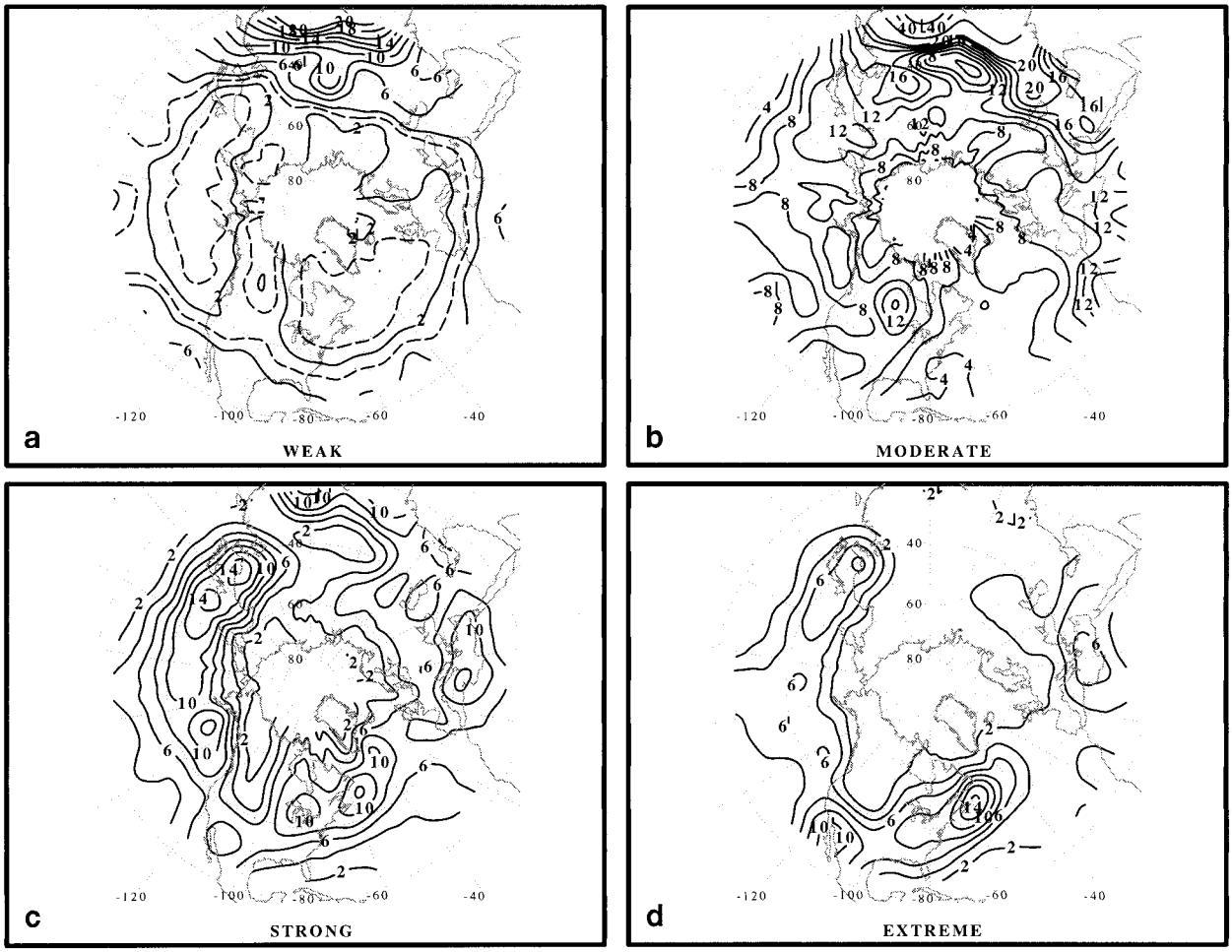

FIG. 3. Percentage of data times with occurrences of 500-hPa geostrophic relative VM during winter (DJF), 1957–87, for the (a) weak category ($0 < \zeta_g \leq 4 \times 10^{-5}$ s^{-1}), (b) moderate category (4×10^{-5} s$^{-1} < \zeta_g \leq 8 \times 10^{-5}$ s^{-1}), (c) strong category (8×10^{-5} s$^{-1} < \zeta_g \leq 12 \times 10^{-5}$ s^{-1}), and (d) extreme category (12×10^{-5} s$^{-1} < \zeta_g \leq 30 \times 10^{-5}$ s^{-1}). The percentage applies to a 10° lat × 10° long area centered at a point on the map. The contour interval is 2% from 0% to 20% and 10% thereafter; supplemental 1% and 3% contours are given by dashed lines in (a). Latitude and longitude are given by dotted lines every 20°.

western Pacific Ocean, with a weaker trough extending from western Russia to northern Africa. Ridges are located over western North America, Europe, and western China. Prominent geostrophic wind speed maxima are located in the base of the North American trough (the Atlantic jet) and the western Pacific Ocean trough (the Pacific jet), in the vicinity of the primary extratropical storm tracks (e.g., Blackmon 1976). A third wind speed maximum extends from northern Africa to southeast Asia, where it connects with the Pacific jet. A notable feature of the entrance region to both the Pacific and Atlantic jets is an upstream extension of the geostrophic wind speed maximum in both the poleward and equatorward directions. This feature suggests climatological flow splitting around the Plateau of Tibet and the Rocky Mountains during winter, with confluence of the split airstreams in the vicinity of the downstream jets.

a. Frequency distributions

To facilitate comparison with previous work (e.g., Sanders 1988; Lefevre and Nielsen-Gammon 1995; Dean and Bosart 1996), results for the geographical distribution of events are expressed as the ratio of the total number of events occurring within a 10° lat × 10° long box centered at each grid point to the total number of data times (hereafter referred to as frequency). Results based on this method compare closely with those based on equal-area averaging, with significant differences (greater than roughly 20%) confined to latitudes poleward of 60°N (not shown).

Weak events tend to occur outside of midlatitudes and are particularly infrequent near jets (Fig. 3a). The largest frequencies, greater than 10%, occur over central and southeast Asia. Values near the Plateau of Tibet may be spurious due to the close proximity of the ground

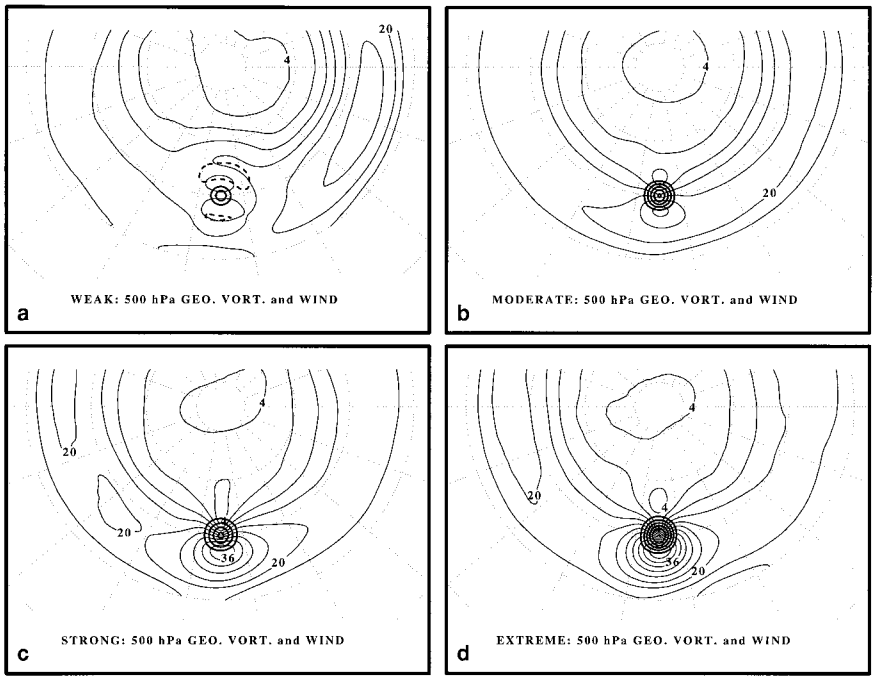

FIG. 4. Mean 500-hPa geostrophic relative vorticity [thick lines: every 1×10^{-5} s^{-1} in (a) and (b); every 2×10^{-5} s^{-1} in (c) and (d)] and geostrophic wind speed (thin solid lines, every 4 m s^{-1}) for 500-hPa vorticity maxima in the (a) weak, (b) moderate, (c) strong, and (d) extreme categories at 40° N. The zero contour is suppressed and latitude and longitude are given by dotted lines every 20°.

to 500 hPa. Potentially significant values of 10%–15% extend from southeast China to the East China Sea, in a region where there is an upstream extension of the Pacific jet (Fig. 2). Other local maxima, such as those over Mongolia and northwestern North America, correspond to regions that have been shown to have a relatively large (small) number of VM genesis (lysis) events (Sanders 1988; Lefevre and Nielsen-Gammon 1995; Dean and Bosart 1996).

Moderate events occur most frequently near the climatological position of the jet from northern Africa across the Middle East to south of the Himalaya region (Fig. 3b). This band of large values merges with another that originates over Mongolia, and the combined band extends across the North Pacific Ocean in the vicinity of the Pacific jet (Figs. 3b and 2). Over North America, moderate-event frequency exhibits a relative minimum over the Rocky Mountains and relative maxima near Lake Winnipeg and the Gulf of California.

Strong and extreme events exhibit relative maxima near Korea and Japan, Newfoundland, the Gulf of California, the Mediterranean Sea, and near the southern end of the Ural mountains (Figs. 3c,d). The maxima over the Mediterranean Sea and Gulf of California are noted for having a relatively high frequency of ''closed cyclone centers'' (Bell and Bosart 1989; Parker et al. 1989). Relative minima are found to the lee of the Rocky Mountains north of 40°N, near the Caspian Sea, over western China, and over southern Greenland.

Focusing on North America, Fig. 3 shows that a relative maximum shifts southeastward away from the Rocky Mountains for increasing amplitude. This transition occurs in a region where the climatological flow proceeds from a ridge over western North America to a trough over eastern North America (Fig. 2). Since the climatological geostrophic relative vorticity increases by only approximately 2×10^{-5} s^{-1} from ridge to trough (not shown), the amplitude increase following the climatological geostrophic streamlines, implied by the results in Fig. 2, must be due to other factors in addition to superposition of the disturbance with the background climatological flow.

b. Spatial structure

The mean spatial structure associated with VM in each category at 40°N is examined here. Owing to the large sample sizes, all anomalies are significant at the 99% level in a Student's *t*-test of significance; therefore significance distributions are not shown on the figures that follow. Results for other latitude bands are similar to those for 40°N that are shown subsequently (Hakim 1997).

The disturbance structure for the weak category ($0 < \zeta_g \leq 4 \times 10^{-5}$ s^{-1}) is that of a weak vorticity center within a ridge of anomalously high heights (Figs. 4a and 5a). The VM appears in the entrance region of a jet, which probably reflects the Pacific jet since a sig-

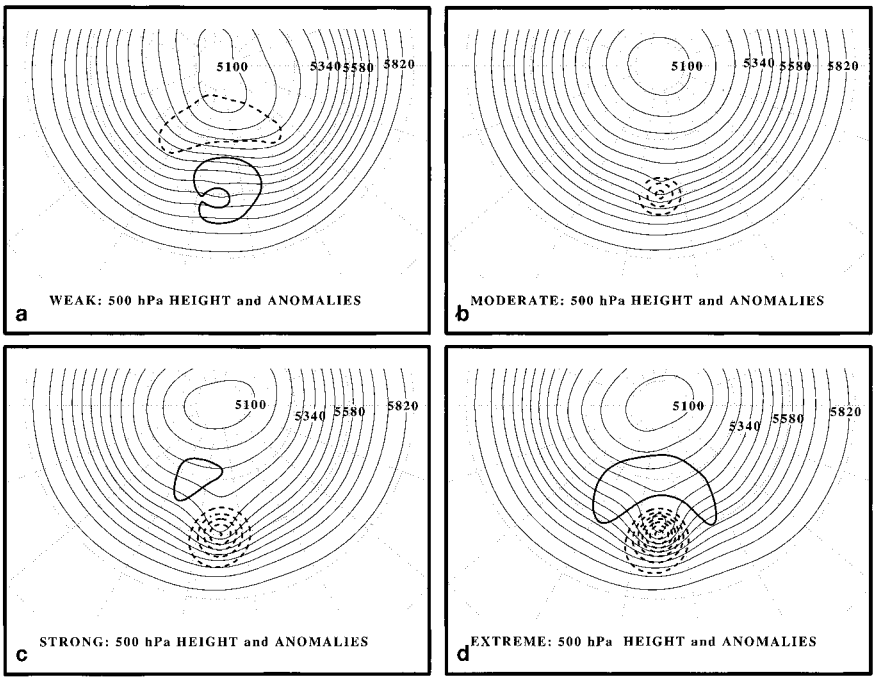

FIG. 5. Mean 500-hPa geopotential height (thin solid lines, every 60 m) and geopotential height anomaly [thick lines: every 20 m in (a) and (b); every 30 m in (c) and (d)] for 500-hPa vorticity maxima in the (a) weak, (b) moderate, (c) strong, and (d) extreme categories at 40° N. The zero contour is suppressed and latitude and longitude are given by dotted lines every 20°.

nificant percentage of the events in this category come from over Asia (Figs. 3a and 4a). A local wind speed maximum south of the VM, a jet streak (e.g., Uccellini and Johnson 1979), appears where the disturbance wind speed of approximately 6 m s^{-1} is in phase with the background flow. Given that the scale of the VM is on the order of the grid spacing, and that most of these events originate in an area where the terrain is near 500 hPa, we do not attribute a high degree of significance to the results for this category.

For the moderate category (4×10^{-5} $s^{-1} < \zeta_g \leq 8 \times 10^{-5}$ s^{-1}), the dominant signature is that of a vortex with a radius (defined below) of approximately 675 km (Figs. 4b and 5b). An approximately 8 m s^{-1} disturbance geostrophic wind speed anomaly superposes on a nearly zonally uniform 20 m s^{-1} westerly background current to yield a localized jet streak to the south of the VM (Fig. 4b). The mean height field shows a weak trough near the VM, and the anomaly height field indicates that moderate VM are localized, without any signature of upstream or downstream anomalies (Fig. 5b).

For the strong category (8×10^{-5} $s^{-1} < \zeta_g \leq 12 \times 10^{-5}$ s^{-1}), the dominant signature is that of a vortex with a radius of approximately 850 km (Figs. 4c and 5c). A broad 40 m s^{-1} jet streak is associated with an anomaly geostrophic wind speed of approximately 14 m s^{-1}. The mean height field reflects an open-wave trough with an anomaly minimum of −153 m. The only anomaly signature aside from the vortices is a slight positive anomaly to the northwest of the VM (Fig. 5c).

For the extreme category (12×10^{-5} $s^{-1} < \zeta_g \leq 30 \times 10^{-5}$ s^{-1}), the structure near the VM is is that of a vortex with a radius of approximately 850 km (Figs. 3d and 4d). The −224-m height anomaly associated with extreme events is sufficient to produce closed height contours (Fig. 5d). A 23 m s^{-1} geostrophic wind speed anomaly superposed on the 20 m s^{-1} background westerly flow yields a prominent jet streak (Fig. 4d).

The anomaly fields for each category are used to make coarse estimates of disturbance properties, which are defined as follows. The disturbance vorticity scale, ζ_0', is given by the composite gridpoint value at the center of the VM, and the background-flow vorticity scale, $\overline{\zeta}_0$, is given by the maximum value of background-flow vorticity on the entire grid. Maximum disturbance geostrophic wind speed is used as a disturbance wind speed scale, U_d. The disturbance length scale is defined by a radius, which is determined by the distance from the VM to a critical value in the four cardinal directions; these are then averaged to yield the mean vortex radius.[8]

[8] If one of the four cardinal direction radii is greater than 1.5 times the average of the other three, it is removed from the mean. This condition prevents contamination of the radius by large excursions in a particular direction of geostrophic relative vorticity contours defining the edge of the vortex.

A critical value of 1×10^{-5} s^{-1} is used rather than zero for the reason that the former value is subjectively determined to provide a more reliable measure of the vortex radius. Alternatively, defining the length scale as the distance from the VM center to the location where the central amplitude decreases by e^{-1} produces results that range from the same value for the weak category to 100 km less than the previous definition for the extreme category. The background-flow wind speed and magnitude of the background-flow deformation listed in Table 1 represent average values for all grid points contained within one disturbance length scale of the VM.

The VM length and wind scales increase with disturbance amplitude (Table 1). Both δ_β and δ indicate that nonlinearity is significant for these disturbances, particularly for the strong and extreme categories, while the Rossby numbers suggest that these disturbances still fall in the QG regime. The order of magnitude difference between the disturbance vorticity and the magnitude of the mean background-flow deformation suggests that, on average, the vortices are not likely to be destroyed by strain in the background-flow wind field (e.g., McWilliams 1984).[9]

The main results of the 33-winter climatology are the following.

- Strong and extreme VM events occur in the storm track regions. Moderate VM occur primarily upstream of the storm tracks, and weak VM events occur over the subtropics, over southeast Asia, near the Plateau of Tibet, and near the Rocky Mountains (Fig. 3).
- The structure of the VM is primarily that of a vortex with little to no large-scale signal. To determine whether there may have been cancellation of large-scale signals due to averaging events over all longitudes, two additional composites based on limited zonal windows were examined for the moderate events: 90°–180°E, and 180°–90°W. The results of these tests are very similar to the control, with the exception that height anomalies for the 90°–180°E events are weaker than the 180°–90°W events (not shown).
- A jet streak is found to the south of the VM and is most noticeable when, on average, the VM is located just north of the main belt of the westerlies such that the vortex wind speed superposes with the maximum westerly background flow (Fig. 4).
- Estimates of the importance of nonlinearity, indicate a range from roughly $O(1)$ for weak events to $O(10)$ for the extreme events.
- Aside from a scale increase with amplitude, there is little qualitative structural difference between the moderate, strong, and extreme categories. This suggests that the subjectively chosen categories are sufficient to resolve the smooth changes in disturbance structure as a function of amplitude.

Although these results benefit from large sample sizes, they suffer from being limited to a single variable and level, and coarse grid spacing (there are approximately four grid points spanning the average disturbances). In the following section, these results are extended to three dimensions and to all standard variables (e.g., u, v, ω, temperature, and geopotential height), as well as derived variables such as vorticity, PV, and tropopause potential temperature and pressure. The drawback of this extension is a reduction in the size of the geographical area to North America and surroundings, and a reduction in the length of the temporal window to a single winter season, December 1988–February 1989.

5. ERICA-period composites

The 3-month mean 500-hPa geopotential height field for the ERICA period is broadly similar to the climatological mean with a trough (ridge) over eastern (western) North America (cf. Figs. 6 and 2). However, during the ERICA period there was a pronounced meridionally oriented height-anomaly couplet over eastern North America, and a positive height anomaly over the Gulf of Alaska (Fig. 6a). Three-month mean tropopause potential temperature and pressure fields largely resemble the 500-hPa geopotential height field, with the lowest tropopause potential temperature and highest tropopause pressure located in the trough over northeastern North America (Figs. 6c,d). However, since jets are typically based at the tropopause rather than at 500 hPa, a sharper and slightly different description of the Atlantic jet is apparent in the tropopause potential temperature and pressure maps (cf. Figs. 6b,c with Fig. 2a). The primary differences are the concentrated gradients of potential temperature and pressure from the Gulf of California across Mexico and the southeastern United States that suggest a subtropical jet leading into the Atlantic jet.

a. Frequency distributions

There are a total of 7457 weak events, 5905 moderate events, 2988 strong events, and 2297 extreme events; a total of 18 647 events for all categories. Two important distinctions between the composites and the climatological study make them only superficially comparable. First, the total-wind relative vorticity is used here, as compared to the geostrophic relative vorticity in the climatology. Second, the resolution here is $1° \times 1°$ as compared to $2.5° \times 2.5°$ in the climatology. These two differences suggest that there is not necessarily any relationship between the categories for these two studies.

[9] However, a caveat to this interpretation is that the background-flow strain averaged over individual events may not be well approximated by the strain in the averaged background flow. The former is difficult to estimate since it requires separating disturbance and background flow for each event.

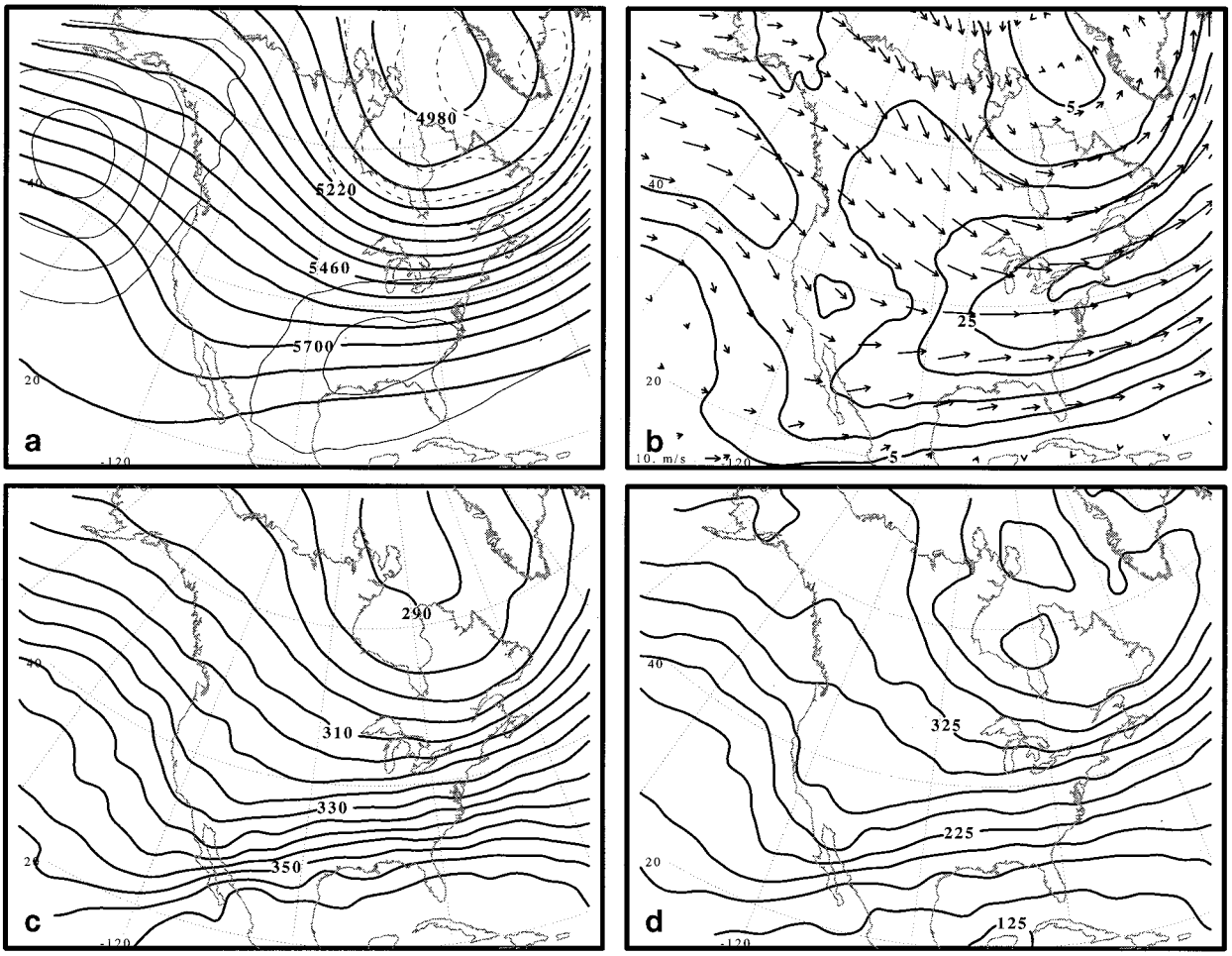

FIG. 6. Time-mean fields for the ERICA period (Dec 1988–Feb 1989): (a) mean 500-hPa geopotential height (thick solid lines, every 60 m) and departure from the 33-yr mean (thin lines, every 30 m); (b) mean 500-hPa vector total wind (arrows, with 10 m s^{-1} reference arrow in the lower left-hand corner) and magnitude of the 500-hPa total wind (solid lines, every 5 m s^{-1}); (c) mean tropopause potential temperature (solid lines every 5 K); and (d) mean tropopause pressure (solid lines every 25 hPa). Latitude and longitude are given by dotted lines every 20°.

However, general properties involving relative amplitude, rather than specific categories, are likely to remain comparable.

Disturbances in the moderate, strong, and extreme categories occur most frequently, about 50%–70% of the time within a 10° × 10° box centered on a point, in the regions associated with the extratropical storm tracks (Fig. 7).[10] A fairly continuous path of large values begins in the Gulf of Alaska, follows the western edge of North America to a local maximum near the northern Gulf of California, proceeds northeastward to another local maximum just to the east of the Rocky Mountains, continues eastward toward the Canadian Maritimes, and finally northeastward to southeast of the southern tip of Greenland. A secondary path of large values begins near the western edge of the Northwest Territories and extends southeastward to join the main path of large values over the Great Lakes region. Another notable large-frequency location is southern Hudson Bay and James Bay. Notable frequency minima are located mainly on the anticyclonic side of the westerlies near the ridge over the eastern Pacific and from the Gulf of Mexico across the subtropical Atlantic Ocean. Overall, these results are quite similar to the smooth patterns shown in Fig. 3.

Although these results do not represent VM track density, the aforementioned large-value paths are suggestive of preferred routes for VM as they approach and cross North America. The primary path suggests that the most likely location for a VM to cross the Rocky Mountains is over the southwestern United States (i.e., southern Arizona, New Mexico, and Texas) near a col in the Rocky Mountain chain and the location of the

[10] Weak events are excluded here because they occur mainly over the subtropics, and their inclusion obscures comparison with the climatological results.

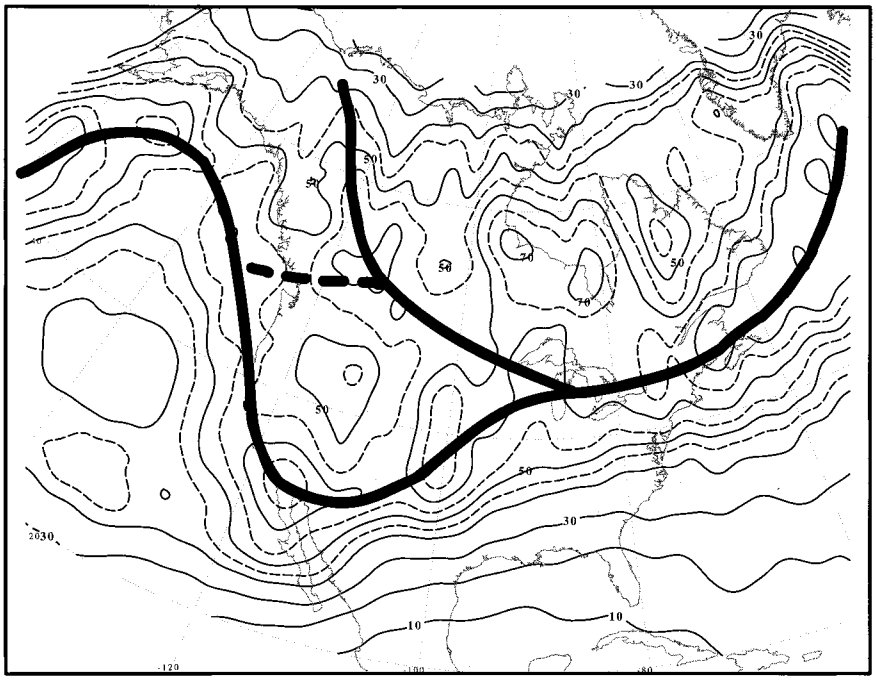

FIG. 7. Percentage of 500-hPa VM in the range 4–30 $\times$ 10^{-5} s^{-1}, occurring during the ERICA period. The percentage (thin lines, every 5%) applies to a 10° lat $\times$ 10° long box centered at a point on the map. The primary and secondary pathways discussed in the text are given by the bold lines.

entrance region to the Atlantic jet. Another possible climatologically favorable location for VM to cross the Rocky Mountains is located near southern British Columbia, where there is a weak connection between the main and secondary paths. It is unclear from these results whether the secondary path reflects amplifying disturbances that have moved equatorward from polar regions, disturbances that have survived a mountain crossing from the Gulf of Alaska, or a location where VM originates (Sanders 1988; Lefevre and Nielsen-Gammon 1995; Dean and Bosart 1996).

b. Spatial structure

For the composite domain, a subset of the full data area is used since data surrounding the VM is needed to allow for a significant compositing region. The total number of events in each composite category are 1635 weak events, 1620 moderate events, 1039 strong events, and 932 extreme events. Anomaly fields are computed from the December 1988–February 1989 mean fields.

The 500-hPa height and relative vorticity for the composite weak VM are very similar to those for the climatological weak VM (cf. Fig. 8a with 4a): these VM are embedded within a larger-scale ridge of higher heights and anticyclonic vorticity. On the tropopause, the signature of the disturbance is a slight undulation of the isentropes, amounting to a -2 K local anomaly when compared to the larger area for which the potential temperature anomalies are 2–4 K (Fig. 9a).

As is the case for the climatological results, moderate disturbances are distinctly different from weak disturbances, exhibiting the structure of a localized VM with a jet streak to the south of the VM (Fig. 8b). On the tropopause, the VM is located near a minor undulation in the 310 K contour and a region of -4 to -8 K anomaly (Fig. 9b). This disturbance does not have sufficient amplitude to produce closed contours and therefore does not pass a basic CS test. However, it is interesting to note the existence of closed contours of EPV on tropospheric isentropic surfaces (not shown).

Strong disturbances exhibit a localized VM with a 24 m s^{-1} jet streak south of the VM (Fig. 8c). Tropopause potential temperature anomalies of -8 to -12 K near the disturbance are associated with a closed 304 K contour in the mean field (Fig. 9c). Extreme disturbances exhibit a localized VM with a 32 m s^{-1} jet streak south of the VM (Fig. 8d). The tropopause potential temperature field exhibits closed contours, with 8 K (293–301 K) ''isolated'' from the lower values north of the disturbance and an anomaly minimum value of -22 K (Fig. 9d).

With regard to geostrophic approximations to the total wind for these disturbances, we note that plots of the geostrophic wind are very similar to those shown in Fig. 8; maximum geostrophic wind speeds in the jet streaks exceed the total wind speed by 0.4, 1.0, 2.4, and 6.3 m s^{-1}, for the weak, moderate, strong, and extreme categories, respectively (not shown). Further comparisons

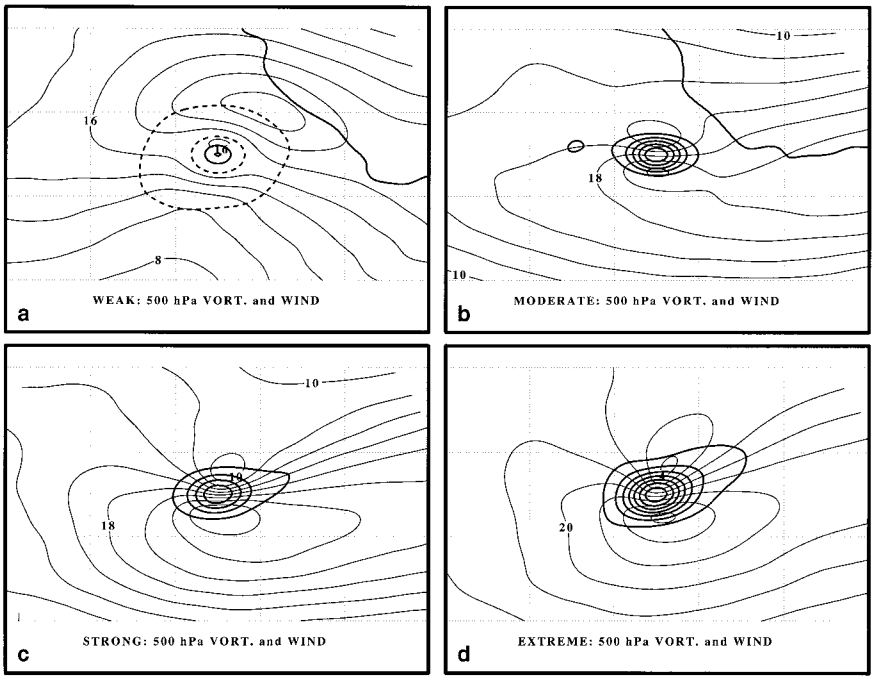

FIG. 8. Mean 500-hPa total-wind relative vorticity [thick lines: every 1×10^{-5} s^{-1} in (a) and (b); every 2×10^{-5} s^{-1} in (c) and (d)] and total-wind speed (thin solid lines, every 4 m s^{-1}) for 500-hPa VM in the (a) weak, (b) moderate, (c) strong, and (d) extreme categories. The zero contour is suppressed and latitude and longitude are given by dotted lines every 10°.

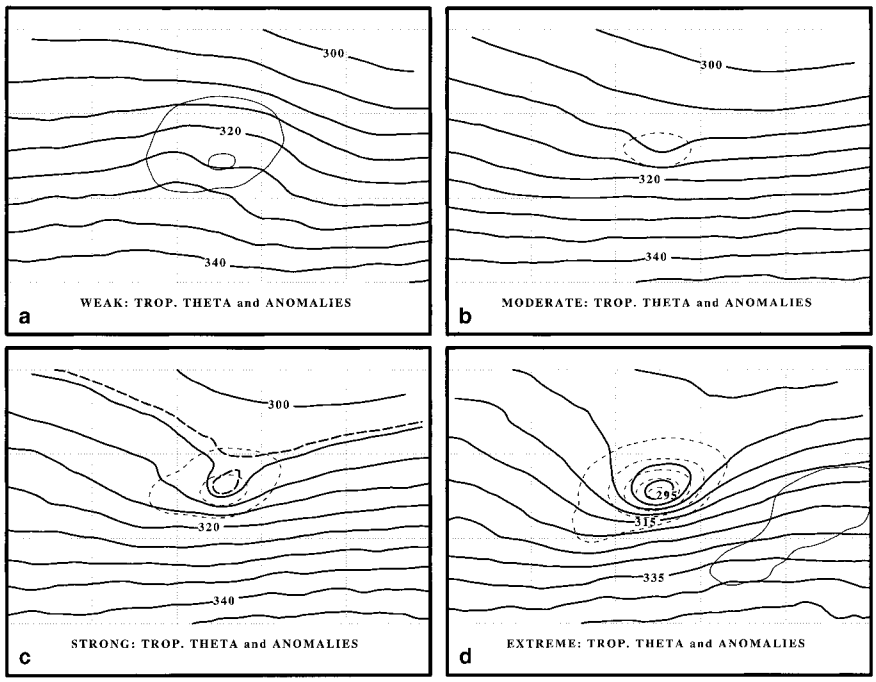

FIG. 9. Mean tropopause potential temperature (solid lines, every 5 K) and anomaly (thin lines, every 4 K) for the ERICA-period climatology. The zero contour is suppressed and latitude and longitude are given by dotted lines every 10°.

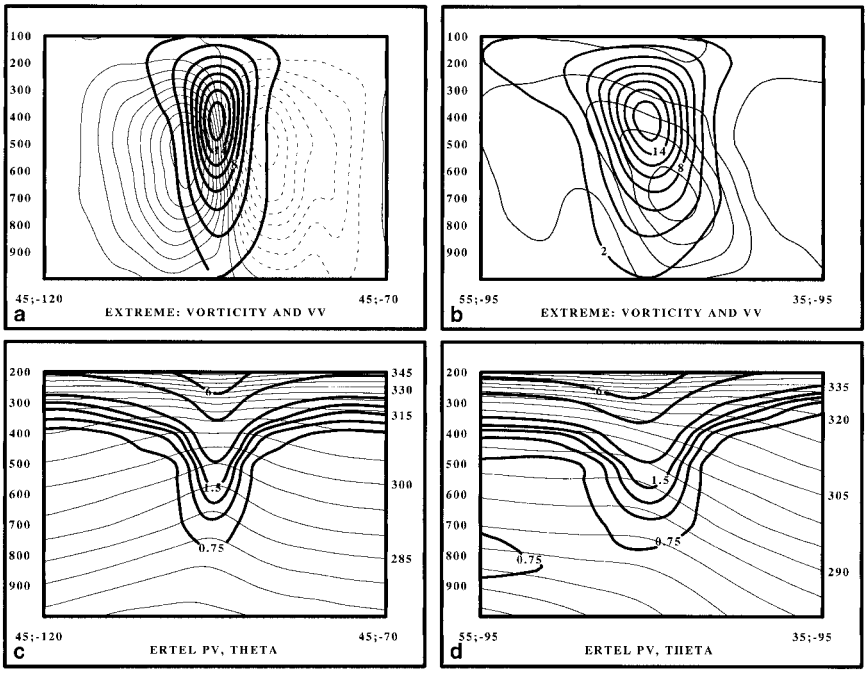

FIG. 10. Cross sections through the extreme category VM: (a) and (b) relative vorticity (thick lines, every 2×10^{-5} s^{-1}), vertical motion (thin lines, every 0.25×10^{-1} Pa s^{-1}); (c) and (d) EPV (thick lines, contours of 0.75, 1.0, 1.25, 1.5, 2, 4, 6, and 8.5 PVU), and potential temperature (thin lines, every 5 K): (a) and (c) zonal cross sections, (b) and (d) meridional cross sections.

of the geostrophic vorticity and QGPV show that they also compare closely with the total-wind quantities (Hakim 1997).

Zonal and meridional cross sections through the extreme VM illustrate the three-dimensional structure (Fig. 10). The VM has maximum amplitude at 400 hPa, with a vertical orientation in the zonal direction and a slight poleward tilt (Figs. 10a,b). There is a sloping dipole in the vertical motion field with rising motion downstream and sinking motion upstream of the VM in the zonal direction (Fig. 10a). This sloping cell appears as sinking motion in the meridional direction, with vortex-tube stretching implied in the vicinity of the VM (Fig. 10b). While the tropopause potential temperature chart indicates closed contours of EPV (1.5 PVU) on the 293–301 K isentropes, the cross sections suggest closed contours of EPV over approximately the 280–340 K isentropic layer; isentropic maps of EPV confirm this inference (not shown).[11] Thus, although tropopause potential temperature is useful for determining when a disturbance is strong enough to close contours on that surface, it does not necessarily indicate the isentropic depth over which closed contours of EPV are present.

The zonal cross section through the composite extreme disturbance compares well with the idealized cold-core upper-cyclone of Thorpe (1986; his Fig. 1). The Thorpe disturbance has a tropopause potential temperature anomaly of -24 K and a relative VM of approximately 14×10^{-5} s^{-1}, as compared with -22 K and 16×10^{-5} s^{-1} for the extreme VM composite. The main differences between these vortices are a larger length scale and weaker horizontal decay with distance for the Thorpe vortex as compared to the extreme VM composite (i.e., these disturbances have different PV–streamfunction relationships).

On average, the composite PV fields suggest that tropopause-level fluid particles are trapped by strong and extreme VM. Another estimate of fluid trapping is given by the fraction of disturbances in each category that occur with (match) a local minimum in tropopause potential temperature in the range 250–330 K. A VM event is declared a *match* with a local minimum in tropopause potential temperature if the two points are separated by less than 300 km (subjectively chosen distance). An estimate of the relative significance of these results is derived from a comparison with results from the same test applied to a second set of events given by a random sample. The random sample is constructed for each category by using the latitude and longitude of each event and generating a random date during the ERICA period to replace the actual date of the event. With this method, the random sample has the same spatial frequency distribution as the actual sample for each category, given

[11] Note that the EPV field shown in Fig. 10 represents a composite average of individual EPV fields. The EPV distribution corresponding to the composite average (u, v, θ) fields is very similar.

TABLE 2. Percentage of composite events in the 500-hPa amplitude categories occurring with (matching) relative minima in tropopause potential temperature and relative maxima in 1000-hPa total-wind relative vorticity. The relative minima in tropopause potential temperature and relative maxima in 1000-hPa total-wind relative vorticity are restricted to occur within 300 km of the 500-hPa total-wind relative vorticity maximum. Percentages for a random sample having the same frequency distributions as the 500-hPa relative vorticity maxima for each category are given in parentheses.

Category	θ_{trop} minimum	ζ (1000) maximum
Weak	8.2% (7.5%)	1.2% (2.0%)
Moderate	19% (11%)	5.3% (4.5%)
Strong	38% (13%)	13% (5.8%)
Extreme	51% (13%)	24% (6.9%)

in Fig. 7, since only the date (not the lat–long) of each event is randomized.

Weak events occur with local minima in tropopause potential temperature during the ERICA period 8.2% of the time as compared to 7.5% for the random sample (Table 2). For moderate events, the matching percentage increases to 19% as compared to 11% for the random sample. The random samples for both strong and extreme events occur with local minima in tropopause potential temperature 13% of the time as compared to 38% and 51%, respectively, for actual events in these categories. The difference between the percentages for actual events and random events increases with disturbance strength and indicates greater confidence in the results for the strong and extreme categories. Composite tropopause potential temperature for extreme events that occur with local minima in tropopause potential temperature compare closely with the full extreme category (cf. Figs. 11a, 9d). In contrast, extreme events that do not occur with local minima in tropopause potential temperature have an open wave structure with a weaker and broader tropopause potential temperature anomaly field (Fig. 11b).

Another component to the analysis of the composite events is an estimation of the CS parameters; the analysis is employed at 500 and 300 hPa by the method outlined in section 4b. Nonlinearity estimates for the strong and extreme disturbances at 500 hPa (300 hPa) range from $\delta = 5.7$ (3.6) to $\delta = 9.8$ (5.5), respectively, with comparable values for δ_β (Table 3). These results indicate that even O(1) nonlinearity is not sufficient to ensure closed PV contours at tropopause level, as indicated from the moderate tropopause potential temperature field (Fig. 9b). The length scale at 500 hPa (300 hPa) increases with amplitude from 330 (400) km for the moderate category to 550 (570) km for the extreme category. As was the case for the 33-winter climatology, the mean magnitude of the background-flow geostrophic deformation is small for all categories.

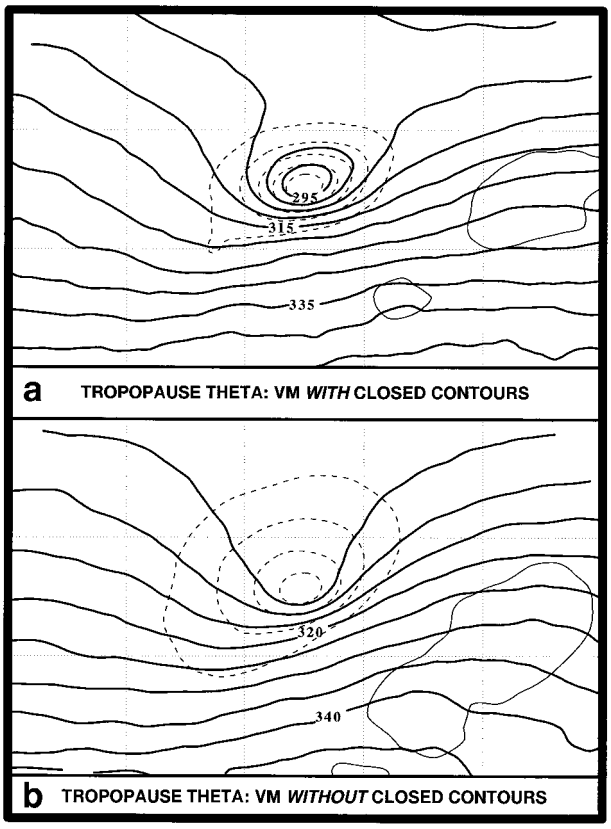

FIG. 11. Mean tropopause potential temperature (solid line, every 5 K) and tropopause potential temperature anomaly (thin lines, every 4 K) for extreme category ERICA-period events that (a) occurred within 300 km of local tropopause potential temperature minima, and (b) did not occur within 300 km of local tropopause potential temperature minima. The zero contour is suppressed and latitude and longitude are given by dotted lines every 10°.

A scatterplot of nondimensional QGPV against nondimensional QG streamfunction for the extreme category disturbance at 500 hPa shows a nearly steady structure (Fig. 12). The scatterplot for a steady structure would have all points falling on one or more curves, indicative of a functional relationship between PV and

TABLE 3. Scale estimates and nondimensional parameters for ERICA anomaly fields. Disturbance parameters are maximum geostrophic wind speed, U_d (m s^{-1}), and length scale, L (km). Nondimensional parameters are nonlinearity, $\delta_\beta = U_d/\beta L^2$ and $\delta = \zeta'/\overline{\zeta}$; magnitude of the background-flow total deformation, $\overline{D}$; and Rossby number, U_d/fL. Here, $f = 10^{-4}$ s^{-1} and $\beta = 1.5 \times 10^{-11}$ m^{-1} s^{-1}. Values apply at 500 hPa, except for those in parentheses, which apply at 300 hPa.

Category	U_d	L	δ_β	δ	$\overline{D}$	Ro
Moderate	7.1 (12)	330 (400)	4.3 (4.8)	3.4 (2.0)	0.6 (0.7)	0.22 (0.29)
Strong	9.0 (43)	480 (670)	2.6 (1.7)	5.7 (3.6)	0.5 (0.7)	0.19 (0.17)
Extreme	33 (43)	550 (570)	7.3 (8.8)	9.8 (5.5)	0.4 (0.6)	0.60 (0.75)

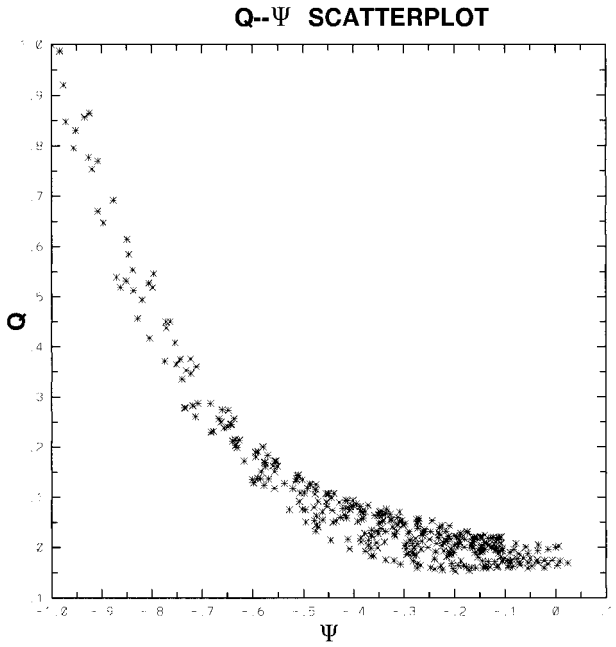

FIG. 12. Scatterplot of nondimensional QGPV with respect to nondimensional geostrophic streamfunction for the extreme-category disturbance at 500 hPa.

streamfunction. The nearly linear relationship in the core of the disturbance (nondimensional QGPV greater than approximately 0.2) is suggestive of a modon solution. However, other vortex solutions, such as a Gaussian vortex, have a nearly linear relationship in the vortex core (e.g., Hopfinger and van Heijst 1993, their Fig. 2). Therefore, this test does not provide sufficient evidence to identify a particular preferred solution type for the extreme category.

As discussed previously, a property distinguishing CSs from RWs is a dependence of disturbance speed on amplitude. Here, a 12-h mean VM speed is determined from 6 h-lagged composites. This speed is compared with the wind speed at the center of the VM, which is considered a background-flow speed since the wind associated with the vortex is approximately zero at this location. Background-flow relative speeds, $c - U$, for the moderate, strong, and extreme VM are -6.7, -7.4, and -8.6 m s^{-1}, respectively. Most of this relative motion is in the zonal direction, with a northward relative motion of less than 1 m s^{-1} in all cases. Therefore, the VM move slightly north of west relative to the background flow, with larger-amplitude disturbances moving westward the fastest. Since these speeds fall in the range of linear RW phase speeds, the modon-with-rider solution is precluded as a potential model for these disturbances (modons translate eastward, or westward, faster than the gravest RW).

As discussed in the introduction, upper-level disturbances are often important for exciting surface cyclones. The extreme VM composite cross sections indicate that surface cyclones do not accompany these 500-hPa VM on average (Fig. 10a). The subsequent analysis aims to determine the spatial distribution of surface cyclones near North America, as well as the proportion of surface cyclones that occur with 500-hPa VM as a function of the categories defined here. Surface cyclones are defined here as local maxima in the 1000-hPa total-wind relative vorticity field in the range 8–30 $\times$ 10^{-5} s^{-1} (hereafter referred to as cyclones) and are identified by the same method used to find 500-hPa VM. The threshold value of 8 $\times$ 10^{-5} s^{-1} was determined subjectively by trial and error; however, the results are not sensitive to this exact value. This method yields a total of 2969 surface cyclone events over the data area during the ERICA period.

Cyclone frequency is similar to extreme VM frequency over the eastern Pacific Ocean and western Atlantic Ocean (cf. Figs. 13 and 7). Specifically, a band of large values, greater than approximately 20%, follows the coastline of western North America before terminating along the California coastline (Fig. 13). While the extreme VM category exhibits a band of large values along the same path, in that case a relative maximum is reached near the northern end of the Gulf of California and the path continues across the continent (Fig. 7). In contrast, cyclone frequency does not exhibit such a path across the United States, with values over most land areas less than 5% (Fig. 13). A second path of large values begins along the East Coast of North America and extends eastward over the western Atlantic Ocean in the vicinity of the climatological storm track. From a local maximum of 40% south of Newfoundland, the path continues along two separate branches, one eastnortheastward and the other northward. The northward path leads to the largest values, greater than 50%, along the west and southeast coasts of Greenland.

Other local frequency maxima are found over the Yukon Territories, Hudson Bay, Great Lakes, and southwestern Gulf of Mexico. These results are in broad agreement with those shown in Zishka and Smith (1980, their Fig. 2a) for January cyclones, 1950–77, with the following two exceptions. Their results show local maxima near Montana and southwestern Kansas, which are not evident here, and the local maximum over Hudson Bay in the present work is not as prominent in their results. Given the different methods between this study and Zishka and Smith (1980), such as defining cyclones by 1000-hPa relative vorticity as opposed to mean sea level pressure, and a single winter season (December–February) as opposed to 28 Januaries, the noted differences may be considered to be relatively minor. Furthermore, there is broad agreement in the results over the storm track east of the North American coastline.

The matching method used earlier is employed here to make an estimate of the fraction of 500-hPa VM that occur with surface cyclones. Here, 500-hPa VM are matched with 1000-hPa cyclones within 300 km of the VM; random-sample results are also generated for com-

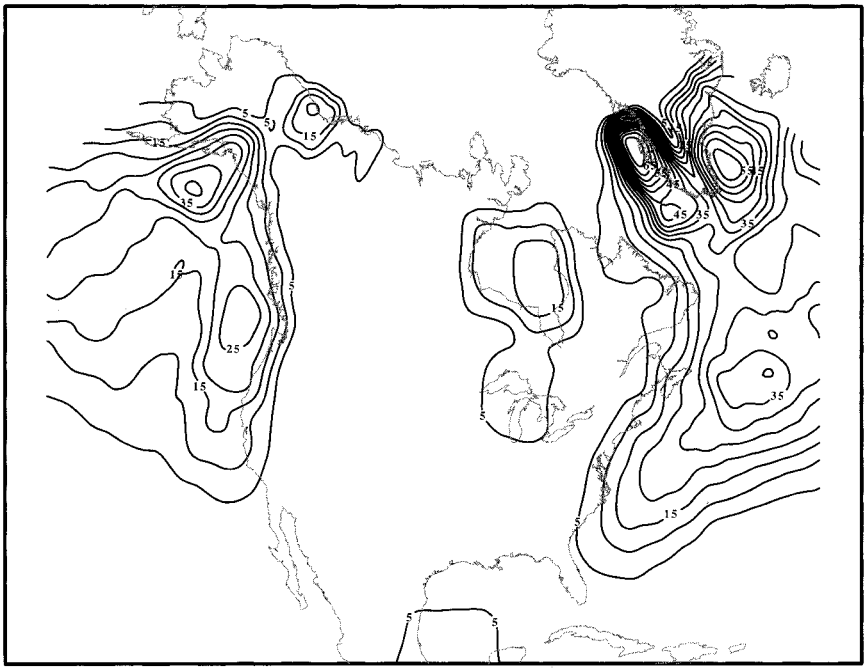

FIG. 13. Percentage of ERICA-period 1000-hPa VM in the range 8–30 $\times$ 10^{-5} s^{-1}. The percentage (shown every 5%) applies to a 10° lat $\times$ 10° long box centered at a point on the map.

parison. Weak VM are associated with cyclones only 1.2% of the time, which is actually less than 2.0% for the random sample (Table 2). This may be due to the fact that weak VM are embedded within larger-scale anticyclones. Moderate VM are associated with cyclones 5.3% of the time, which does not differ significantly from the value of 4.5% for the random sample. In contrast, strong and extreme VM are associated with cyclones 13% and 24% of the time, respectively, as compared with only 5.8% and 6.9% for random samples, respectively. Extending the match distance to 600 km indicates that weak, moderate, strong, and extreme (random) events are associated with cyclones 4.2% (7.5%), 13% (13%), 25% (18%), and 41% (21%), respectively. For a 600-km matching distance, strong and extreme events account for 32% of cyclones as compared with 17% of cyclones for a 300-km matching distance. Since only the strong and extreme VM exhibit CS properties, we estimate that CS VM occur with approximately one-third of all surface cyclones. This conclusion is tempered by the earlier caveat regarding comparing the Eulerian perspective adopted here with a pseudo-Lagrangian disturbance definition. Furthermore, we note that the amplitude of the 500-hPa VM prior to surface cyclone development may not be the same as the amplitude at the time of the matching results.

Finally, we note a possible limitation of this work concerns the fact that the composite fields could potentially be interpreted as an average over a population of waves, with the localized structure resulting from a cancellation of waves with different wavelengths. For simplicity, consider the vorticity field for a one-dimensional problem [$\zeta(x)$]. Let the sample population comprise waves, with a normal probability density function having mean k_0 and variance σ^2. The expected value is

$$\overline{\zeta}(x) = e^{-\sigma^2 x^2/2} \cos(k_0 x). \tag{6}$$

Here, x is taken to be nondimensional zonal distance along 45°N lat. For certain choices of k_0 and σ, such as $k_0 = 6$ and $\sigma = 5$, $\overline{\zeta}(x)$ gives the appearance of a local VM with a radius of about 500 km (not shown). Thus, as with all compositing-based studies, a connection to individual cases needs to be made to ensure that the results are not an artifact of the compositing procedure. In this regard, Hakim (1997) examined individual events during the ERICA period and found that the main results contained herein correspond closely with those for the individual cases.

6. Conclusions

A diagnostic method, based on the theory of nonlinear waves and vortices, is developed and applied to observations to test the hypothesis that some tropopause-based perturbations, such as cyclogenesis precursor disturbances, are nonlinear coherent structures (CSs) as opposed to quasi-linear Rossby waves. The diagnostic method is designed to determine the following disturbance properties: nonlinearity, QGPV–streamfunction relationship, speed, and trapping of fluid particles. These tests are applied to observations of relative vorticity maxima (VM) for a 33-winter climatology at 500 hPa

and three-dimensional composites for a single winter season. In addition to testing the CS hypothesis, another goal of this work is to assess whether observed disturbances tend toward a preferred structure; candidate solutions considered here are solitary waves, modons, and monopolar vortices.

Results for a 33-winter climatological study indicate that VM occur most frequently over and upstream from the main oceanic storm tracks. Frequency minima are located near major topographical barriers, such as the Rocky Mountains, Greenland, and the Plateau of Tibet. The mean structure of the disturbances is a vortex with a radius of approximately 500–800 km. A jet streak is located south of the vortex, due to a superposition of the vortex-induced wind with the westerly background flow. Nonlinearity is $O(1)$ or greater for all categories.

Results for a composite study agree with those of the climatology: 500-hPa total-wind relative VM exhibit the structure of localized cyclonic vortices with length scales of approximately 350–600 km. A zonal cross section of anomaly vertical motion for the extreme events exhibits a vertically tilted dipole, which suggests that the vertical circulation may act to oppose the tendency of the background-flow vertical shear to tip the vortex from its vertical orientation. A demonstration of this effect in idealized numerical simulations of vortices in vertical shear is given by Jones (1995).

Nonlinearity for the composite study is $O(1)$ or greater for all categories. However, closed contours of tropopause potential temperature require $\delta \approx 5$, which corresponds to tropopause potential temperature anomalies of approximately -8 K and to relative VM at 500 hPa greater than approximately 8×10^{-5} s^{-1}. This result precludes linear (e.g., Rossby waves) and weakly nonlinear waves (e.g., solitary waves) as potential models for these disturbances. The range of isentropes that exhibit closed contours of Ertel PV (EPV) is proportional to the amplitude of the disturbance. The moderate composite category exhibits closed EPV contours over a narrow range of isentropes located in the upper troposphere, whereas the strong and extreme composites exhibit closed EPV contours through a larger range of isentropes, particularly in the lower stratosphere for the extreme category. Thus, these vortices have a variable vertical structure that suggests the greatest probability for trapping fluid particles exists on tropospheric isentropes.

The composite disturbances translate slightly north of west at 6–9 m s^{-1} relative to the background flow. Since this speed falls in the range of linear Rossby wave speeds, the modon-with-rider and solitary wave solutions cannot serve as models for these disturbances. The speed results are qualitatively consistent with the theory for the motion of unsteady cyclonic vortices on a β plane, which predicts that they move northwestward. There is also agreement with the prediction of Adem (1956) that the westward component of vortex motion increases with vortex radius, since the strong and extreme VM have larger radii and westward speeds when compared with the moderate VM. Given the aforementioned evidence, we conclude that these disturbances are, on average, unsteady nonlinear monopolar vortices. This result highlights a need for further research into the dynamics of vortices in the presence of background flows comprising regions with locally enhanced gradients of wind speed and potential vorticity (i.e., jets).

Since explosive cyclogenesis events tend to occur in association with large-amplitude 500-hPa VM (e.g., Sanders 1986), it is possible that CSs, such as the those determined by the composite strong and extreme categories, may play a more important role in this subset of cyclones as compared to all cyclones. In this regard, Sanders (1986, 1987) found that the rate of development of explosively developing cyclones (''bombs'') was proportional to 500-hPa absolute vorticity advection. Furthermore, this vorticity advection is attributed to a 500-hPa vorticity maximum, which is often present many days prior to the surface development. In a compositing study of bomb cyclones, Manobianco (1989) found a prominent localized VM upstream from the developing surface cyclone. The maximum total-wind relative vorticity of 13×10^{-5} s^{-1} and the VM structure are very similar to the extreme category (cf. Manobianco 1989, his Fig. 2, with Fig. 8d). Takayabu (1991) documented a case of cyclogenesis involving an upper-level vortex that has a radius of approximately 400–500 km and a relative VM of 13×10^{-5} s^{-1}; again, these properties compare closely to the extreme category. Takayabu also examined rapidly developing cyclones [maximum sea-level deepening rates greater than 7 hPa (12 h)$^{-1}$] occurring in the vicinity of the Japan Islands during 1986, and found seven out of 39 cases involve a ''coupling development'' between upper and lower vortices.

Acknowledgments. This work represents a portion of the author's Ph.D. dissertation, completed at the University at Albany, State University of New York. The support of the author's advisors, Professors Daniel Keyser and Lance Bosart, is gratefully acknowledged. The ERICA-period data were obtained from ECMWF through the National Center for Atmospheric Research (NCAR) by Prof. Gary Lackmann (College at Brockport, State University of New York). Thoughtful discussions during the course of this work with Mr. Philip Cunningham (University at Albany), Profs. Bosart and Keyser, and Drs. Chris Snyder and Richard Rotunno (NCAR) are greatly appreciated. Manuscript reviews by Drs. Rotunno, Snyder, Christopher Davis (NCAR), and three anonymous referees were helpful in clarifying portions of the paper. This research was supported by NSF Grants ATM-9114598, ATM-9413012, and ATM-9421678, awarded to the University at Albany, State University of New York.

APPENDIX

Overview of Solitary Wave and Modon Solutions

a. Solitary waves

For a frame of reference moving at speed c, the transformation $X = x - ct$ allows (2) to be expressed as

$$J(\psi' + cy + \overline{\psi}, \nabla^2\psi' + \beta y + \overline{\psi}_{yy}) = 0. \quad \text{(A1)}$$

The streamfunction has been separated by $\psi = \overline{\psi}(y) + \psi'(X, y)$. Scaling of (A1) proceeds with the following nondimensional parameters: $(X, y) \sim (L\hat{X}, L\hat{y})$, $\psi' \sim UL\hat{\psi}$, $\overline{\psi} \sim \lambda L\hat{\overline{\psi}}$, $c \sim \lambda\hat{c}$. Expanding the Jacobian in (A1) and dropping the hat and prime notation, (A1) becomes

$$\delta_\beta\epsilon^2 J(\psi, \psi_{XX}) + \delta_\beta J(\psi, \psi_{yy}) + \psi_X(1 + \overline{\psi}_{yyy}) - \epsilon^2(c + \overline{\psi}_y)\psi_{XXX} - (c + \overline{\psi}_y)\psi_{XyY} = 0. \quad \text{(A2)}$$

The parameter $\epsilon = L/L_x$ represents the anisotropy of the solution and will be small (<1) by assumption, and we take $\lambda = \beta L^2$. For solitary waves to exist, nonlinearity and dispersion must balance; this requires $\epsilon^2 = \delta_\beta$ (Malanotte-Rizzoli and Hendershot 1980). Approximate solutions of (A2) are obtained for small δ_β by expanding ψ and c in terms of δ_β: $\psi = \psi_0 + \delta_\beta\psi_1 + \cdots; c = c_0 + \delta_\beta c_1 + \cdots$. Separation of variables at leading order by $\psi_0 = \Psi(X)\Phi(y)$, with $\Phi(0) = \Phi(1) = 0$, yields an eigenvalue problem for the meridional structure and zeroth-order disturbance speed:

$$\Phi_{yy} - \Lambda_0(y)\Phi = 0. \quad \text{(A3)}$$

The function $\Lambda_0(y)$, given by

$$\Lambda_0(y) = \frac{\overline{u}_{yy} - \beta}{\overline{u} - c_0} = -\frac{\overline{\zeta}_y}{\overline{u} - c_0} = \frac{d\overline{\zeta}}{d\overline{\psi}^*}, \quad \text{(A4)}$$

where $\overline{\psi}^* = \overline{\psi} + c_0 y$, is a weighting (or potential) function that determines the meridional structure of the disturbance [i.e., the solution of (A3)]. As noted by Malguzzi and Malanotte-Rizzoli (1984), solitary waves require $\Lambda_0(y)$ to have a minimum in y. Butchart et al. (1989) detail the importance of this potential well for confining (trapping) the meridional disturbance structure and draw an analogy with the time-independent Schrödinger equation for an electron trapped in an electrostatic potential well. Butchart et al. also show that a similar interpretation applies in the zonal direction, with the distinction that the disturbance is trapped by itself rather than by the background flow.

The zonal structure function, $\Psi(X)$, is recovered at next order through a solvability condition that is satisfied by multiplying the $O(\delta_\beta)$ equation by Φ, integrating in y and setting the result to zero; the result is the steady Korteweg-deVries (KdV) equation:

$$\Psi_X + \frac{a_1}{c_1}\Psi\Psi_X + \frac{a_2}{c_1}\Psi_{XXX} = 0. \quad \text{(A5)}$$

The constants a_1 and a_2 depend on Λ_0 and Φ. A solution of (A5) is

$$\Psi(X) = \text{sgn}(a_1a_2)A\,\text{sech}^2\left(\frac{X}{W}\right). \quad \text{(A6)}$$

Here, sgn(x) denotes the sign of argument x, $W^{-2} = (1/12)|a_1/a_2|A$, where W is the *width* of the solitary wave, and $c_1 = -\text{sgn}(a_1a_2)a_1A/3$ is the correction to the wave speed.

b. Modons

Channel boundary conditions in y are replaced with $\psi \to 0$ for $r \to \infty$, where $r = \sqrt{X^2 + y^2}$. A polar coordinate form of the steady reference frame introduced in (A1) is used here, with $X = r\cos\theta$ and $y = r\sin\theta$. The governing equation in these coordinates has a solution of the form

$$\nabla^2\psi + \beta y = F(\psi + cy), \quad \text{(A7)}$$

where $F(\alpha)$ is an unspecified functional. The solution domain is divided into a near field and a far field by a circle with radius $r = a$. The boundary condition suggests that the far-field structure of F has the form $F(\alpha) = \alpha\beta c^{-1} \equiv \alpha p^2$, which allows for the proper decay of the solution at large r. Substituting into (A7) the linear relation for $F(\alpha)$ in the far field and assuming $F(\alpha) = -k^2\alpha$ in the near field gives[12]

$$\nabla^2\psi + k^2\psi = -(k^2 + p^2)\,cr\sin\theta, \qquad r < a \quad \text{(A8a)}$$

$$\nabla^2\psi - p^2\psi = 0, \qquad r > a. \quad \text{(A8b)}$$

One solution is

$$\psi(r, \theta) = ca\left[\frac{p^2J_1(kr)}{k^2J_1(ka)} - \left(1 + \frac{p^2}{k^2}\right)\frac{r}{a}\right]\sin\theta \qquad r < a, \quad \text{(A9a)}$$

$$\psi(r, \theta) = -ca\left[\frac{K_1(pr)}{K_1(pa)}\right]\sin\theta \qquad r > a. \quad \text{(A9b)}$$

Here, J_1 is the first-order Bessel function of the first kind and K_1 is the first-order modified Bessel function of the second kind.

Although monopolar solutions are not possible in isolation, they can be superposed with the dipole solution (A9); for this reason, these monopolar fields are called *riders* (Flierl et al. 1980). Rider fields, denoted by a subscripted R, are given by

$$\psi_R(r) = \psi_R(0)J_0(kr), \qquad r < a \quad \text{(A10a)}$$

$$\psi_R(r) = \psi_R(0)\left[\frac{kJ_1(ka)}{pK_1(pa)}\right]K_0(pr) \qquad r > a. \quad \text{(A10b)}$$

[12] The constants k and p are referred to as the modon interior and exterior wavenumbers, respectively.

Here, k and p are the wavenumbers corresponding to a modon solution (A9) and $\psi_R(0)$ is an amplitude parameter. Although all structural characteristics of rider fields are determined by the modon solution (i.e., k and p), an important aspect of (A10) is that the amplitude parameter is free. This freedom permits monopoles of arbitrary amplitude to be superposed on the modons such that the signature of the total solution, $\psi + \psi_R$, can appear to be that of a nearly axisymmetric monopole.

REFERENCES

Adem, J., 1956: A series solution for the barotropic vorticity equation and its application in the study of atmospheric vortices. *Tellus,* **8,** 364–372.

Bell, G. D., and L. F. Bosart, 1989: A 15-year climatology of Northern Hemisphere 500 mb closed cyclone and anticyclone centers. *Mon. Wea. Rev.,* **117,** 2142–2163.

Berestov, A. L., 1979: Solitary Rossby waves. *Izv. Acad. Sci. USSR Atmos. Oceanic Phys.,* **15,** 443–447.

——, 1981: Some new solutions for the Rossby solitons. *Izv. Acad. Sci. USSR Atmos. Oceanic Phys.,* **17,** 60–64.

Blackmon, M. L., 1976: A climatological spectral study of the 500 mb geopotential height of the Northern Hemisphere. *J. Atmos. Sci.,* **33,** 1607–1623.

——, J. M. Wallace, N.-C. Lau, and S. L. Mullen, 1977: An observational study of the Northern Hemisphere wintertime circulation. *J. Atmos. Sci.,* **34,** 1040–1053.

——, Y.-H. Lee, and J. M. Wallace, 1984a: Horizontal structure of 500 mb height fluctuations with long, intermediate and short time scales. *J. Atmos. Sci.,* **41,** 961–980.

——, ——, ——, and H.-H. Hsu, 1984b: Time variation of 500 mb height fluctuations with long, intermediate and short time scales as deduced from lag-correlation statistics. *J. Atmos. Sci.,* **41,** 981–991.

Bleck, R., 1990: Depiction of upper/lower vortex interaction associated with extratropical cyclogenesis. *Mon. Wea. Rev.,* **118,** 573–585.

Bosart, L. F., G. J. Hakim, K. R. Tyle, M. A. Bedrick, W. E. Bracken, M. J. Dickinson, and D. M. Schultz, 1996: Large-scale antecedent conditions associated with the 12–14 March 1993 cyclone (''Superstorm '93'') over eastern North America. *Mon. Wea. Rev.,* **124,** 1865–1891.

Boyle, J. B., and L. F. Bosart, 1986: Cyclone–anticyclone couplets over North America. Part II: Analysis of a major cyclone event over the eastern United States. *Mon. Wea. Rev.,* **114,** 2432–2465.

Butchart, N., K. Haines, and J. C. Marshall, 1989: A theoretical and diagnostic study of solitary waves and atmospheric blocking. *J. Atmos. Sci.,* **46,** 2063–2078.

Chang, E. K. M., 1993: Downstream development of baroclinic waves as inferred from regression analysis. *J. Atmos. Sci.,* **50,** 2038–2053.

——, and I. Orlanski, 1993: On the dynamics of a storm track. *J. Atmos. Sci.,* **50,** 999–1015.

Charney, J. G., 1947: The dynamics of long waves in a baroclinic westerly current. *J. Meteor.,* **4,** 135–162.

Davey, M. K., and P. D. Killworth, 1984: Isolated waves and eddies in a shallow water model. *J. Phys. Oceanogr.,* **14,** 1047–1064.

Davis, C. A., and K. A. Emanuel, 1991: Potential vorticity diagnostics of cyclogenesis. *Mon. Wea. Rev.,* **119,** 1929–1953.

Dean, D. B., and L. F. Bosart, 1996: Northern Hemisphere 500-hPa trough merger and fracture: A climatology and case study. *Mon. Wea. Rev.,* **124,** 2644–2671.

Eady, E. T., 1949: Long waves and cyclone waves. *Tellus,* **1,** 33–52.

Ek, N. R., and G. E. Swaters, 1994: Geostrophic scatter diagrams and the application of quasigeostrophic free-mode theory to a northeast Pacific blocking episode. *J. Atmos. Sci.,* **51,** 563–581.

Farrell, B., 1984: Modal and non-modal baroclinic waves. *J. Atmos. Sci.,* **41,** 668–673.

——, 1985: Transient growth of damped baroclinic waves. *J. Atmos. Sci.,* **42,** 2718–2727.

——, 1989: Unstable baroclinic modes damped by Ekman dissipation. *J. Atmos. Sci.,* **46,** 397–401.

Flierl, G. R., 1977: The application of linear quasigeostrophic dynamics to Gulf Stream rings. *J. Phys. Oceanogr.,* **7,** 365–379.

——, 1987: Isolated eddy models in geophysics. *Annu. Rev. Fluid Mech.,* **19,** 493–530.

——, V. D. Larichev, J. C. McWilliams, and G. M. Reznik, 1980: The dynamics of baroclinic and barotropic solitary eddies. *Dyn. Atmos. Oceans,* **5,** 1–41.

Gall, R. L., 1976a: A comparison of linear baroclinic instability theory with the eddy statistics of a general circulation model. *J. Atmos. Sci.,* **33,** 349–373.

——, 1976b: Structural changes of growing baroclinic waves. *J. Atmos. Sci.,* **33,** 374–390.

Guinn, T. A., and W. H. Schubert, 1993: Hurricane spiral bands. *J. Atmos. Sci.,* **50,** 3380–3403.

Haines, K., and P. Malanotte-Rizzoli, 1991: Isolated anomalies in westerly jet streams: A unified approach. *J. Atmos. Sci.,* **48,** 510–526.

——, ——, and M. Morgan, 1993: Persistent jet stream intensifications: A comparison between theory and data. *J. Atmos. Sci.,* **50,** 145–154.

Hakim, G. J., 1997: Extratropical cyclogenesis in terms of baroclinic vortex dynamics. Ph.D. dissertation, University at Albany, State University of New York, 210 pp. [Available from Dept. of Earth and Atmospheric Sciences, University at Albany, SUNY, Albany, NY 12222.]

——, L. F. Bosart, and D. Keyser, 1995: The Ohio Valley wave-merger cyclogenesis event of 25–26 January 1978. Part I: Multiscale case study. *Mon. Wea. Rev.,* **123,** 2663–2692.

——, D. Keyser, and L. F. Bosart, 1996: The Ohio Valley wave-merger cyclogenesis event of 25–26 January 1978. Part II: Diagnosis using quasigeostrophic potential vorticity inversion. *Mon. Wea. Rev.,* **124,** 2176–2205.

Haupt, S. E., J. C. McWilliams, and J. J. Tribbia, 1993: Modons in shear flow. *J. Atmos. Sci.,* **50,** 1181–1198.

Hollingsworth, A., D. B. Shaw, P. Lönnberg, L. Illari, K. Arpe, and A. J. Simmons, 1986: Monitoring of observation and analysis quality by a data assimilation system. *Mon. Wea. Rev.,* **114,** 861–879.

Hopfinger, E. J., and G. J. F. van Heijst, 1993: Vortices in rotating fluids. *Annu. Rev. Fluid Mech.,* **25,** 241–289.

Hoskins, B. J., M. E. McIntyre, and A. W. Robertson, 1985: On the use and significance of isentropic potential vorticity maps. *Quart. J. Roy. Meteor. Soc.,* **111,** 877–946.

Jones, S. C., 1995: The evolution of vortices in vertical shear. Part I: Initially barotropic vortices. *Quart. J. Roy. Meteor. Soc.,* **121,** 821–851.

Kamenkovich, V. M., M. N. Koshlyakov, and A. S. Monin, Eds., 1986: *Synoptic Eddies in the Ocean.* D. Reidel, 433 pp.

Kizner, Z. I., 1984: Rossby solitons with axisymmetric baroclinic modes. *Dokl. Akad. Nauk SSSR,* **275,** 1495–1498.

Larichev, V. D., and G. M. Reznik, 1976: Two-dimensional solitary Rossby waves. *Dokl. Akad. Nauk SSSR,* **231,** 12–13.

Lee, S., and I. M. Held, 1993: Baroclinic wave packets in models and observations. *J. Atmos. Sci.,* **50,** 1413–1428.

Lefevre, R. J., and J. W. Nielsen-Gammon, 1995: An objective climatology of mobile troughs in the Northern Hemisphere. *Tellus,* **47A,** 638–655.

Lim, G. H., and J. M. Wallace, 1991: Structure and evolution of baroclinic waves as inferred from regression analysis. *J. Atmos. Sci.,* **48,** 1718–1732.

Malanotte-Rizzoli, P., 1982: Planetary solitary waves in geophysical flows. *Advances in Geophysics,* Vol. 24, Academic Press, 147–224.

——, and M. C. Hendershot, 1980: Solitary Rossby waves over var-

iable relief and their stability. Part I: The analytical theory. *Dyn. Atmos. Oceans,* **4,** 247–260.
Malguzzi, P., and P. Malanotte-Rizzoli, 1984: Nonlinear stationary Rossby waves on nonuniform zonal winds and atmospheric blocking. Part I: The analytical theory. *J. Atmos. Sci.,* **41,** 2620–2628.
Manobianco, J., 1989: Explosive East Coast cyclogenesis over the west-central North Atlantic Ocean: A composite study derived from ECMWF operational analyses. *Mon. Wea. Rev.,* **117,** 2365–2383.
Mass, C. F., H. J. Edmond, H. J. Friedman, N. R. Cheney, and E. E. Recker, 1987: The use of compact discs for the storage of large meteorological and oceanographic data sets. *Bull. Amer. Meteor. Soc.,* **68,** 1556–1558.
McWilliams, J. C., 1980: An application of equivalent modons to atmospheric blocking. *Dyn. Atmos. Oceans,* **5,** 43–66.
——, 1984: The emergence of isolated coherent vortices in turbulent flow. *J. Fluid Mech.,* **146,** 21–43.
——, 1991: Geostrophic vortices. *Nonlinear Topics in Ocean Physics,* Elsevier, 996 pp.
Neven, E. C., 1994: Baroclinic modons on a sphere. *J. Atmos. Sci.,* **51,** 1447–1464.
Nielsen-Gammon, J. W., and R. J. Lefevre, 1996: Piecewise tendency diagnosis of dynamical processes governing the development of an upper-tropospheric mobile trough. *J. Atmos. Sci.,* **53,** 3120–3142.
Ogura, Y., and H.-M. H. Juang, 1990: A case study of rapid cyclogenesis over Canada. Part I: Diagnostic study. *Mon. Wea. Rev.,* **118,** 655–672.
Orlanski, I., and J. J. Katzfey, 1991: The life cycle of a cyclone wave in the Southern Hemisphere. Part I: Eddy energy budget. *J. Atmos. Sci.,* **48,** 1972–1998.
——, and E. K. M. Chang, 1993: Ageostrophic geopotential fluxes in downstream and upstream development of baroclinic waves. *J. Atmos. Sci.,* **50,** 212–225.
——, and J. P. Sheldon, 1993: A case of downstream baroclinic development over western North America. *Mon. Wea. Rev.,* **121,** 2929–2950.
——, and ——, 1995: Stages in the energetics of baroclinic systems. *Tellus,* **47A,** 605–628.
Parker, S. S., J. T. Hawes, S. J. Colucci, and B. P. Hayden, 1989: Climatology of 500 mb cyclones and anticyclones, 1950–85. *Mon. Wea. Rev.,* **117,** 558–570.
Pedlosky, J., 1987: *Geophysical Fluid Dynamics.* 2d ed. Springer-Verlag, 710 pp.
Reed, R. J., M. T. Stoelinga, and Y.-H. Kuo, 1992: A model-aided study of the origin and evolution of the anomalously high potential vorticity in the inner region of a rapidly deepening marine cyclone. *Mon. Wea. Rev.,* **120,** 893–913.
Rhines, P. B., 1975: Waves and turbulence on the β-plane. *J. Fluid Mech.,* **69,** 417–443.
Saffman, P. G., 1992: *Vortex Dynamics.* Cambridge University Press, 311 pp.
Sanders, F., 1986: Explosive cyclogenesis in the west-central North Atlantic Ocean, 1981–1984. Part I: Composite structure and mean behavior. *Mon. Wea. Rev.,* **114,** 1781–1794.
——, 1987: A study of 500 mb vorticity maxima crossing the east coast of North America and associated surface cyclogenesis. *Wea. Forecasting,* **2,** 70–83.
——, 1988: Life history of mobile troughs in the upper westerlies. *Mon. Wea. Rev.,* **116,** 2629–2648.
Schär, C., and H. Wernli, 1993: Structure and evolution of an isolated semi-geostrophic cyclone. *Quart. J. Roy. Meteor. Soc.,* **119,** 57–90.
Shepherd, T. G., 1987: Rossby waves and two-dimensional turbulence in a large-scale zonal jet. *J. Fluid Mech.,* **183,** 467–509.
Simmons, A. J., and B. J. Hoskins, 1976: Baroclinic instability on the sphere: Normal modes of the primitive and quasi-geostrophic equations. *J. Atmos. Sci.,* **33,** 1454–1477.
——, and ——, 1977: Baroclinic instability on the sphere: Solutions with a more realistic tropopause. *J. Atmos. Sci.,* **34,** 581–589.
——, and ——, 1979: The downstream and upstream development of unstable baroclinic waves. *J. Atmos. Sci.,* **36,** 1239–1254.
Swenson, M., 1982: Isolated 2D vortices in the presence of shear. Summer study program in geophysical fluid dynamics. Woods Hole Oceanographic Inst. Tech. Rep. WHOI-82-45, 324–336. [Available from Woods Hole Oceanographic Institution, Woods Hole, MA 02543.]
Takayabu, I., 1991: ''Coupling development'': An efficient mechanism for the development of extratropical cyclones. *J. Meteor. Soc. Japan,* **69,** 837–841.
——, 1992: Supplement to ''Coupling development'': Accelerative development of extratropical cyclones by using finite amplitude initial disturbances. *J. Meteor. Soc. Japan,* **70,** 609–628.
Thorpe, A. J., 1986: Synoptic scale disturbances with circular symmetry. *Mon. Wea. Rev.,* **114,** 1384–1389.
Tribbia, J. J., 1984: Modons in spherical geometry. *Geophys. Astrophys. Fluid Dyn.,* **30,** 131–168.
Uccellini, L. W., and D. R. Johnson, 1979: The coupling of upper and lower tropospheric jet streaks and implications for the development of severe convective storms. *Mon. Wea. Rev.,* **107,** 682–703.
——, D. Keyser, K. F. Brill, and C. H. Wash, 1985: The Presidents' Day cyclone of 18–19 February 1979: Influence of upstream trough amplification and associated tropopause folding on rapid cyclogenesis. *Mon. Wea. Rev.,* **113,** 962–988.
Verkley, W. T. M., 1984: The construction of barotropic modons on a sphere. *J. Atmos. Sci.,* **41,** 2492–2504.
——, 1987: Stationary barotropic modons in westerly background flows. *J. Atmos. Sci.,* **44,** 2383–2398.
Wallace, J. M., G.-H. Lim, and M. L. Blackmon, 1988: Relationship between cyclone tracks, anticyclone tracks and baroclinic waveguides. *J. Atmos. Sci.,* **45,** 439–462.
Zishka, K. M., and P. J. Smith, 1980: The climatology of cyclones and anticyclones over North America and surrounding ocean environs for January and July, 1950–1977. *Mon. Wea. Rev.,* **108,** 387–401.